

## **Section 1**

Assimilation of atmospheric and land  
observations.

Data impact and sensitivity studies.

Methodological advances.



# Application of 1DVAR Technique using Ground-based Microwave Radiometer Data to Estimating Thermodynamic Environments in Winter Convective Clouds

Kentaro Araki<sup>1</sup>

*1: Meteorological Research Institute, Tsukuba, Ibaraki, Japan*  
e-mail: araki@mri-jma.go.jp

## 1. Introduction

In winter, convective clouds sometimes develop and cause local snowfalls and lightning strikes in the Kanto plain in Japan. To understand and forecast these winter convective clouds, temporally high-resolution analysis of environmental conditions is required. Recently, in order to understand temporal variations of thermodynamic conditions of convective clouds, one-dimensional variational (1DVAR; Araki et al., 2015) analysis combined with numerical weather model and microwave radiometer (MWR) data has been applied into the cases of convective clouds causing a tornado in spring (e.g., Araki et al., 2014) and causing local heavy rainfalls in summer (e.g., Araki et al., 2017) in the Kanto plain. In this study, we performed a case study on the winter convective clouds on 26 January 2019, and examined the temporal variation of environmental conditions and features of convective clouds by using Japan Meteorological Agency (JMA) analysis data, dense surface meteorological observation data, Himawari-8 data, JMA operational radar data, disdrometer and MWR data obtained at the Meteorological Research Institute (MRI) in Tsukuba, Ibaraki.

## 2. Temporal variation of thermodynamic environment of winter convective clouds

In this study, a ground-based multi-channel MWR (MP-3000, Radiometrics) installed at the MRI in Tsukuba (36.05°N, 140.13°E) is used for analysis of atmospheric environments and microphysical properties of convective clouds. The MWR measures the brightness temperatures of 21 K-band (22–30 GHz) and 14 V-band (51–59 GHz) microwave channels with the band width of 300 MHz in zenith direction. Vertical profiles of atmospheric temperature and water vapor density were retrieved by the 1DVAR (Araki et al., 2015) technique combining the MWR observation data and the results of the JMA Non-Hydrostatic Model (NHM) simulations. A rain sensor is combined with the MWR, and the MWR data at the time of rain was not used for the retrievals. A numerical experiment was performed using the NHM with a horizontal grid spacing of 1 km and a model domain of 500x500 km covering the Kanto plain, and the 18-hour atmospheric conditions were simulated from 06:00 JST (=UTC+9h) on 26 January 2019. The initial and boundary conditions were taken from the 3-hourly JMA mesoscale analyses, and other setups were the same as those used in Saito et al. (2006). The NHM-derived vertical profiles at Tsukuba were interpolated to MWR observation times and used for the 1DVAR retrievals. In this study, the data of a micro rain radar (MRR, METEK) and a disdrometer (Parsivel, OTT) installed at the MRI were also used for the analysis of cloud microphysical properties of the convective clouds.

On 26 January, the surface pressure pattern was the winter monsoon type and the upper cold vortex moved to the northern Japan. Since the Kanto plain was located on the southeastern side of the cold vortex, synoptic condition was favorable for convection development in the Kanto plain. In respect of the mesoscale environments, the low-level convergence line was formed in the Kanto plain by west-northwesterly and northerly airflows that crossed the mountain areas (Fig. 1). The Himawari-8 infrared images captured the cloud street associated with the convergence line from 13:30 JST, and radar echoes of convective clouds were observed by the JMA Tokyo radar from 14:40 JST. Two convective clouds developed in the convergence line and passed over Tsukuba from about 15:30 to 16:30 JST. The results of the MRR showed the existence of echo at the altitude of 3–5 km 5–10 minutes before the surface precipitation (Fig. 2a). The disdrometer observed precipitations by two convective clouds from 15:34 to 15:44 JST and from 16:03 to 16:32 JST, and liquid water path (LWP) derived by the MWR significantly increased about 20 minutes before the surface precipitation by the first convective cloud.

To investigate the temporal variation of thermodynamic environments, variations of following stability indices calculated from 1DVAR-derived thermodynamic profiles were examined; precipitable water vapor (PWV), lifted condensation level (LCL), level of free convection (LFC), equilibrium level (EL), convective available potential energy (CAPE), Showalter stability index (SSI), lifted index (LI), and K index (KI). The LCL, LFC, EL and CAPE were calculated under the assumption that the air parcel averaged over 0–500 m altitudes was lifted. From the comparison of PWVs derived from 1DVAR, NHM, and the JMA local analyses, it was indicated that the 1DVAR technique overperform the results of the NHM simulations in the water vapor field and that results of 1DVAR would contain errors due to water clouds from 15:00 to 17:00 JST. As the results, EL increased from 09:00 to 15:00 JST significantly, and LCL and LFC showed similar trends (Fig. 3a). The values of CAPE were 100–900 J kg<sup>-1</sup> before the surface precipitation in Tsukuba (Fig. 3b). Indices of SSI, LI, and KI also showed that thermodynamic environments significantly became unstable before the precipitation in Tsukuba. From the results of temporal variations of retrieved PWVs, low-level and upper temperature fields, it was found that the thermodynamic environments became unstable until 15:00 JST because of the increases of low-level atmospheric temperature and influence of upper cold air flow.

### 3. Conclusions and remarks

In this case, the thermodynamic environments, which were obtained from the 1DVAR technique combined with the MWR data and numerical simulation data, showed unstable atmospheric conditions favorable for the convective cloud development in the Kanto plain prior to the other observations of cloud and precipitation by satellite and radar. These results suggest that the 1DVAR technique using MWR data would be of benefit in nowcasting winter convective clouds causing local snowfalls and lightning strikes. It is desired that the applicability and effectiveness of the 1DVAR technique in the other winter cases are examined in the future.

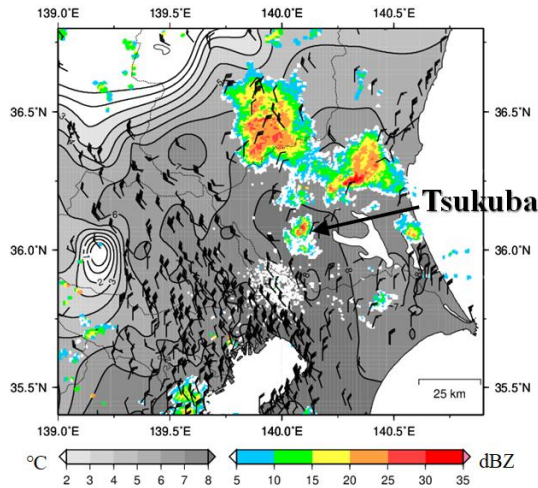


Figure 1. Surface air temperature (gray) and wind (barb) at 15:00 JST derived from the JMA stations and the Atmospheric Environmental Regional Observation System of the Japanese Ministry of the Environment. The PPI reflectivity (color) observed by the Tokyo radar at the elevation angle of 1.1° at 15:32 JST.

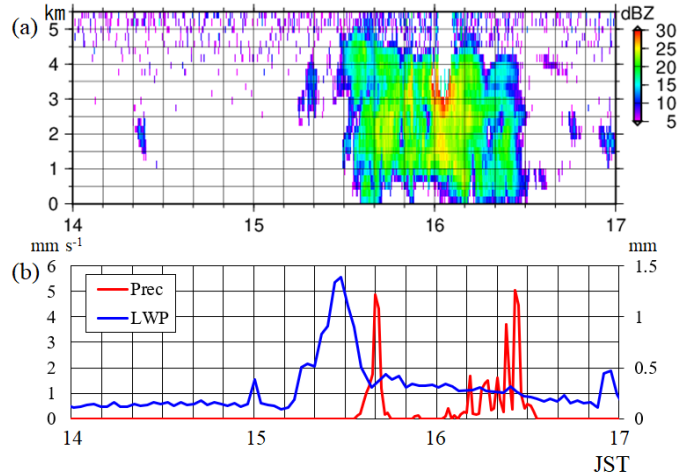


Figure 2. (a) Time-height cross sections of reflectivity derived from MRR and (b) time series of precipitation intensity ( $\text{mm h}^{-1}$ ; red line) derived from the disdrometer and LWP (mm) obtained from the zenith observation by the MWR at the MRI in Tsukuba.

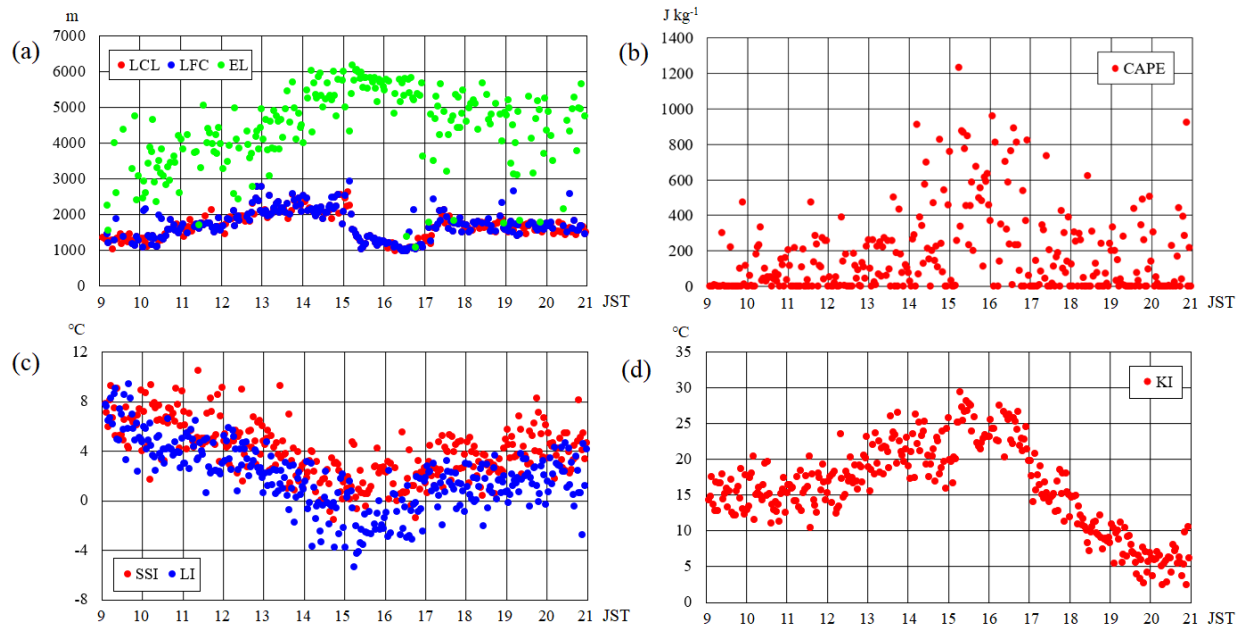


Figure 3. Temporal variations of stability indices of (a) LCL, LFC, EL, (b) CAPE, (c) SSI, LI, and (d) KI calculated by atmospheric thermodynamic profiles derived from the 1DVAR technique.

### References:

- Araki, K., H. Ishimoto, M. Murakami, and T. Tajiri, 2014: Temporal variation of close-proximity soundings within a tornadic supercell environment. *SOLA*, **10**, 57–61.
- Araki, K., M. Murakami, H. Ishimoto, and T. Tajiri, 2015: Ground-based microwave radiometer variational analysis during no-rain and rain conditions. *SOLA*, **11**, 108–112.
- Araki, K., M. Murakami, T. Kato, and T. Tajiri, 2017: Analysis of atmospheric environments for convective cloud development around the Central Mountains in Japan during warm seasons using ground-based microwave radiometer data. *Tenki*, **64**, 19–36.

# Operative Objective Analysis of Productive Moisture Fields in the Top Soil Layer: Day-to-Day Variability

Bykov Ph.L.<sup>1,2)</sup>, Gordin V. A.<sup>2,1)</sup>, Tarasova L.L.<sup>1)</sup>, Vasilenko E.V.<sup>3)</sup>

<sup>1)</sup>Hydrometeorological Centre of Russia, <sup>2)</sup>National Research University – Higher School of Economics, <sup>3)</sup>Research Center “Planeta”

Soil moisture is one of the components of water balance in nature. Traditionally, during the growing season of agricultural crops, hydrometeorological stations evaluate (see e.g. Fig.1) the amount productive moisture located in the layers 0-10, 0-20, 0-50 and 0-100 cm.

We also use information from polar orbital MetOp-A and MetOp-B satellites (and are going to add the information from MetOp-C) with measuring devices – scatterometers ASCAT. Their measurements permit to evaluate humidity in the upper (about 5-cm) soil layer, using remote sensing (ERS). The data is quickly distributed to the meteorological center via the system of data exchange EUMETSAT. We use (see [1]) both types of the information for our daily operative objective analysis (OOA) of soil productive moisture in the top (0-10 cm) and arable (0-20 cm) soil layers, see Fig.1. A considerable part of Russian agricultural areas are located in the European territory, and there is a rather a dense network of Roshydromet stations making observations of the reserves of soil moisture 3 times a month.

Here we compare the fields of our OOA and meteorological fields valid at the same time. We compared the data on soil moisture in the arable layer and precipitation. Days with heavy (more than 20 mm/day) rains were studied here. It was expected that on such days the following "jump" of soil moisture as a function of time would be most evident. Indeed, the soil moisture content increased in about 75% of cases, but it decreased in about 25% of cases. The interaction of the solid part of soil and water, as well as the movement of moisture in the soil can explain this phenomenon. Fig. 1 shows an example of the soil moisture for July 22 2018 and Fig. 2 presents the day-to-day dynamics of soil moisture at the hydrometeorological station Pochinok (Smolensk region).

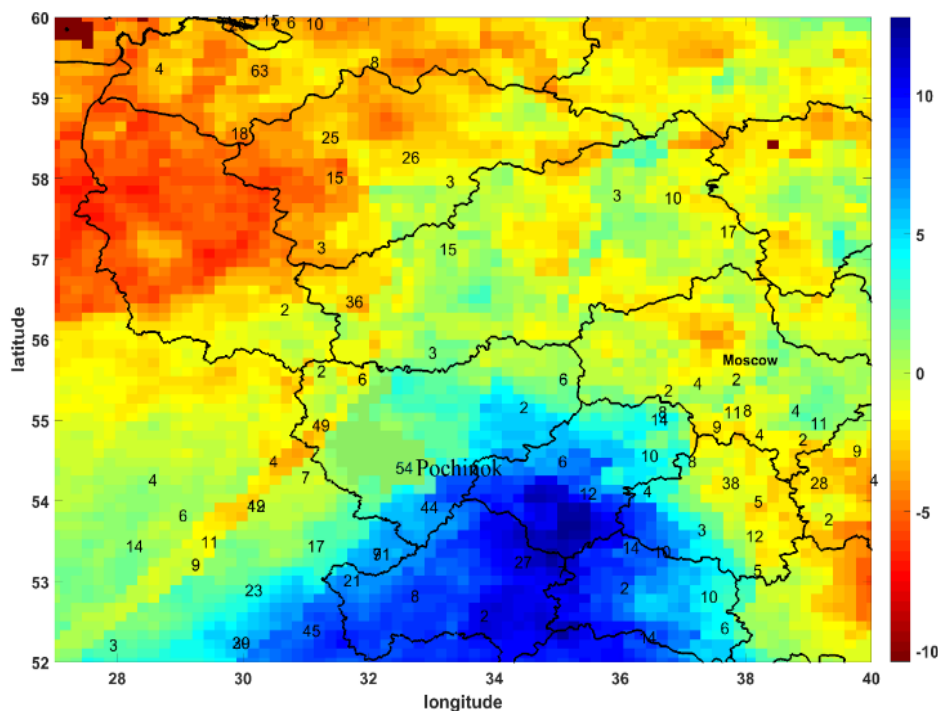


Fig.1. The daily OOA change of productive moisture (mm) in the soil layer [0, 20 cm] on July 22 day 2018 (color). The numbers on the map show the amounts of precipitation (mm) that fell during the day

The moisture movement within the soil depends on the soil humidity. A.A.Rode [2] marks out several categories of forces, which affect the moisture contained in the soil. They are a) gravity (gravitational forces); b) capillary (meniscal) forces or forces of superficial pressure; c) sorption forces, representing a combination of attractions between water molecules and their attraction to soil particles; d) osmotic forces, representing attraction between ions and molecules in the solution and from exchange soil cations. Gravitational forces are constant and always directed down, other forces strongly depend on moisture content in the soil and can have

any direction. When the soil humidity increases, first the adsorptive forces act, trying to approach the maximum adsorptive moisture capacity. Only then, the sorption comes into effect. With humidity increasing and sorption weakening, the capillary forces enter the game. Further, sorption and gravitational forces become commensurable. In this connection, forces of all these three categories can affect together the moisture movement during this interval. Thus, while soil humidity increases, the forces acting on moisture within the soil decrease.

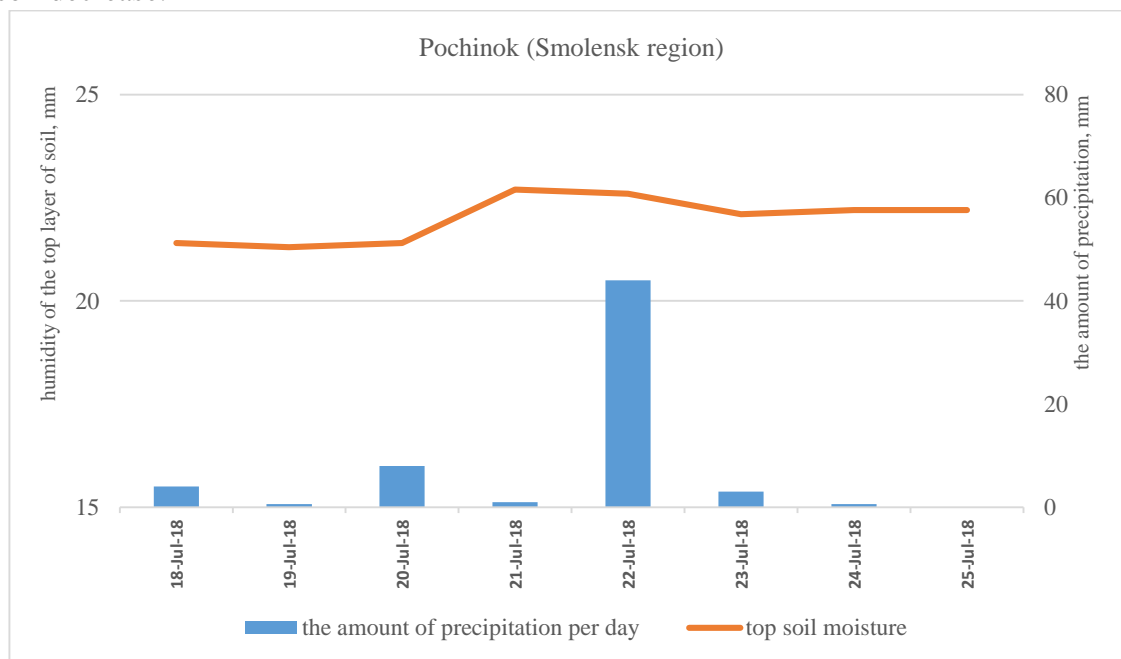


Fig.2. Dynamics of OOA of productive moisture of the top soil layer [0, 20 cm] and the amount of precipitation at the hydrometeorological station Pochinok (Smolensk region).

Therefore, a "jump" of humidity, as a function of time, only in days before which no precipitation was observed.

If even slight rains fell during the preceding period thus filling the soil with moisture, no humidity increase in the top soil layer is observed, since the moisture arriving on the soil surface will flow down into underlying layers.

We investigated also the days with hot dry wind (more exactly: the deficiency of partial pressure of water vapor exceeded 20hPa, and the maximum speed of the surface wind was more than 15 m/s). Under such conditions, the top soil should lose moisture quickly. According to the OOA, a decrease in humidity in days with hot dry winds was not observed except for cases with preceding soil desiccation (relative humidity <20% of the top soil).

Thus, our OOA of productive soil moisture based on the land and satellite observations allows to explain day-to-day variability and to evaluate adequately intra soil moisture fluxes.

Ph.L.Bykov and V.A.Gordin were supported by Academic Fund Program at the National Research University Higher School of Economics (HSE) in 2018 – 2019 (grant № 18-05-0011) and by the Russian Academic Excellence Project «5-100».

### Literature

1. Ph.L.Bykov, E.V.Vasilenko, V.A.Gordin, L.L.Tarasova, Statistical Structure of Topsoil Moisture from Ground-Based and Satellite Data. Russian Meteorology and Hydrology. 2017. No.6, pp. 403–414.
2. A.A. Rode Issues of water regime of soils. Leningrad, Hydrometeoizdat, 1978 (in Russian). 213 p.
3. L.D. Baver 1948. Soil Physics. 2nd Edition. John Wiley & Sons Inc. New York. 398 pp.
4. D. Hillel 1998. Environmental Soil Physics: Fundamentals, Applications, and Environmental Considerations. Academic Press, Oval Road, London, UK. 775 pp.

## **Data Assimilation in the Next-Generation Global Prediction System Era: Initial Implementation of FV3-based Global Forecast System**

Daryl Kleist (NOAA/NWS/NCEP/EMC) & Catherine Thomas (IMSG @ NOAA/NWS/NCEP/EMC)

Email: [daryl.kleist@noaa.gov](mailto:daryl.kleist@noaa.gov) & [catherine.thomas@noaa.gov](mailto:catherine.thomas@noaa.gov)

As part of the Next-Generation Global Prediction System (NGGPS), the National Centers for Environmental Prediction (NCEP) is replacing the spectral dynamical core of the Global Forecast System (GFS) with the Finite-Volume Cubed-Sphere Dynamical Core (FV3) of the Geophysical Fluid Dynamics Laboratory (GFDL). The initial implementation of the FV3-based GFS is focused on incorporating the FV3 core into the existing infrastructure and is tentatively scheduled to go operational in June 2019.

The operational GFS and global data assimilation system (GDAS) utilize a Gridpoint Statistical Interpolation (GSI)-based hybrid 4D Ensemble-Variational solver (4DEnVar, Kleist and Ide, 2015). The system uses a dual resolution configuration, with a deterministic component at T1534 (~13km) horizontal resolution and an 80 member ensemble run at T574 (~35km) horizontal resolution, all which utilize 64 hybrid sigma-pressure vertical layers and a model top of ~55km. The ensemble is updated every cycle utilizing the ensemble square root filter (EnSRF) of Whitaker and Hamill (2002). The hybrid 4DEnVar deterministic analysis is performed on the ensemble grid and is used to replace the EnSRF analysis ensemble mean.

The initial FV3-based GFS implementation seeks to utilize existing infrastructure as much as is feasible. The FV3 dynamic core utilizes a cubed-sphere grid, though with the addition of the NOAA Environmental Modeling System (NEMS) write-grid component, forecasts are also available on the Gaussian lat-lon grids that the GSI and EnKF infrastructure can ingest without much additional effort. This allows for the deterministic and ensemble analysis increments to be computed on the Gaussian grid, which are subsequently interpolated to the cubed-sphere grid within the model itself and added onto the native grid restart state.

The stochastic components that are used in the GFS spectral model have been modified and adapted for use within the NEMS-FV3 model. For the initial implementation, stochastically perturbed boundary layer specific humidity (SHUM, Tompkins and Berner, 2008) and stochastically perturbed physics tendencies (SPPT, Buizza et al., 1999) are targeted for use. Stochastic energy backscatter (SKEBS, Shutts, 2005) is available as an option in the NEMS-FV3 model, but is not utilized as part of this initial implementation.

One significant decision that was made early in the development and testing phase was to increase the spatial resolution of the ensemble to be exactly half of the deterministic control. The prototype FV3-based GFS is configured to run at C768 resolution (~13 km) for the control with an 80 member ensemble cycled at C384 (~26 km). Likewise, the analysis increment is also computed on a Gaussian grid that roughly corresponds to C384 resolution.

The initial FV3-based GFS implementation utilizes physics parameterizations primarily from operations, with the largest exception being the microphysics. The operational prognostic cloud scheme has been replaced with a single moment, six-class cloud microphysics scheme from GFDL (Lin et al., 1983). However, the operational GSI analyzes a total cloud condensate (a description of this within the context of all-sky assimilation can be found in Zhu et al., 2016). For this initial implementation, the cloud liquid water and cloud ice hydrometeors from the background are combined into a total cloud condensate in order to mimic current operations and produce a total cloud analysis increment. However, this increment is never passed back to the model itself, but instead serves as a so-called “sink variable.” In practice, the other control variables are being updated to be consistent with the total cloud increment through the multivariate correlations contained in the background error specification.

Other aspects that have changed from the operational system are turning on all sky assimilation for the Advanced Technology Microwave Sounder (ATMS) instrument, reducing the near-surface sea temperature (NSST) background error correlation length scale, and the omission of tropical cyclone relocation and the full field digital filter. New observations include Geostationary Operational Environmental Satellite (GOES)-16 atmospheric motion vectors, NOAA-20 Cross-track Infrared Sounder (CrIS) and ATMS radiances, additional Infrared Atmospheric Sounding Interferometer (IASI) water vapor channels, Suomi National Polar-orbiting Partnership (NPP) Ozone Mapping Profiler Suite (OMPS) data, and select Meteosat-11 Spinning Enhanced Visible and Infrared Imager (SEVIRI) channels.

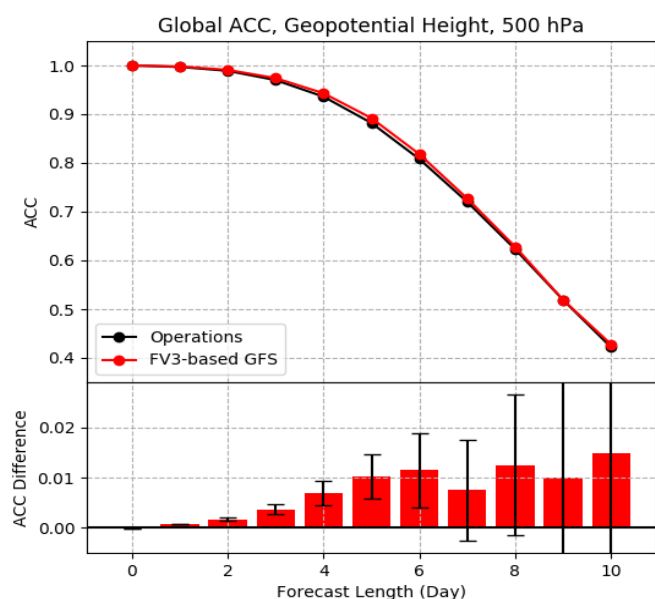


Figure 1: Global time-averaged 500 hPa anomaly correlation coefficients (ACC) as a function of forecast lead time (top) for the operational GFS (black) and the FV3-based GFS real-time parallel (red) with forecasts initialized at 00 UTC for January 27 - April 24, 2019. The bottom panel shows the difference between the FV3-based GFS and the operational GFS for the same timeframe. The error bars represent 95% confidence threshold as derived from a student t-test.

To formally evaluate the full implementation package, several seasons of retrospective parallels were performed and a substantial amount of case studies covering a breadth of high impact meteorological events were examined. Results were predominantly positive, such as the significantly improved anomaly correlation scores (Figure 1), better representation of the wind-pressure relationship in tropical cyclones, precipitation skill, and stratospheric ozone forecasts. Development of the second FV3-based implementation has already begun, with a focus on advanced physics, raising of the model top, and increased vertical resolution.

**Acknowledgements:** The work described in this article contains contributions from many people at NCEP/EMC and ESRL/PSD. We would like to specifically thank Rahul Mahajan, Fanglin Yang, Russ Treadon, Jun Wang, Jeff Whitaker, Phil Pegion, Yanqiu Zhu, and Andrew Collard.

## References

- Buizza, R., M. Miller, and T. N. Palmer, 1999: Stochastic Representation of model uncertainties in the ECMWF Ensemble Prediction System. *Quart. J. Roy. Meteor. Soc.*, **125**, 2887–2908. doi: [10.1002/qj.49712556006](https://doi.org/10.1002/qj.49712556006).
- Kleist, D.T., and K. Ide, 2015: [An OSSE-Based Evaluation of Hybrid Variational–Ensemble Data Assimilation for the NCEP GFS. Part II: 4DEnVar and Hybrid Variants](https://doi.org/10.1175/MWR-D-13-00350.1). *Mon. Wea. Rev.*, **143**, 452–470, doi: [10.1175/MWR-D-13-00350.1](https://doi.org/10.1175/MWR-D-13-00350.1).
- Lin, Y., R.D. Farley, and H.D. Orville, 1983: [Bulk Parameterization of the Snow Field in a Cloud Model](https://doi.org/10.1175/1520-0450(1983)022<1065:BPOTSF>2.0.CO;2). *J. Climate Appl. Meteor.*, **22**, 1065–1092, doi: [10.1175/1520-0450\(1983\)022<1065:BPOTSF>2.0.CO;2](https://doi.org/10.1175/1520-0450(1983)022<1065:BPOTSF>2.0.CO;2).
- Shutts, G., 2005: A kinetic energy backscatter algorithm for use in ensemble prediction systems. *Quart. J. Roy. Meteor. Soc.* **131**, 3079–3102, doi: [10.1256/qj.04.106](https://doi.org/10.1256/qj.04.106).
- Tompkins, A. M., and J. Berner, 2008: A stochastic convective approach to account for model uncertainty due to unresolved humidity variability. *J. Geophys. Res.*, **113**, D18101, doi: [10.1029/2007JD009284](https://doi.org/10.1029/2007JD009284).
- Whitaker, J.S. and T.M. Hamill, 2002: [Ensemble Data Assimilation without Perturbed Observations](https://doi.org/10.1175/1520-0493(2002)130<1913:EDAWPO>2.0.CO;2). *Mon. Wea. Rev.*, **130**, 1913–1924, doi: [10.1175/1520-0493\(2002\)130<1913:EDAWPO>2.0.CO;2](https://doi.org/10.1175/1520-0493(2002)130<1913:EDAWPO>2.0.CO;2).
- Zhu, Y., E. Liu, R. Mahajan, C. Thomas, D. Groff, P. Van Delst, A. Collard, D. Kleist, R. Treadon, and J.C. Derber, 2016: [All-Sky Microwave Radiance Assimilation in NCEP’s GSI Analysis System](https://doi.org/10.1175/MWR-D-15-0445.1). *Mon. Wea. Rev.*, **144**, 4709–4735, doi: [10.1175/MWR-D-15-0445.1](https://doi.org/10.1175/MWR-D-15-0445.1).

# Operational Use of ASCAT Coastal Wind Data in JMA's Mesoscale Data Assimilation System

Shin Koyamatsu

Numerical Prediction Division, Japan Meteorological Agency

E-mail: shin.koyamatsu@met.kishou.go.jp

## 1. Introduction

Assimilation of data on ocean vector winds (OVWs) from the Advanced Scatterometer (ASCAT) onboard the EUMETSAT Metop satellites contributes to the improvement of low-level wind analysis fields in Japan Meteorological Agency (JMA) global and mesoscale numerical weather prediction (NWP) systems (Takahashi 2010, Moriya 2016). To further improve the forecast skill of mesoscale NWP by assimilating higher-resolution wind data, JMA changed the OVW product for mesoscale NWP analysis from ASCAT 25-km winds to ASCAT 12.5-km coastal winds (Verhoef et al. 2012) on March 26 2019. This report outlines the impacts of the assimilation on the NWP system.

## 2. Utilization of coastal OVW data

The settings and parameters of quality control for coastal wind data are identical to those for 25-km OVWs. Spatial thinning of 0.5 degrees (approximately 50 km) was applied to both products, but a clear difference is seen in the spatial coverage of the OVWs used (Figure 1). As the target area of the JMA mesoscale NWP system includes many islands and coastal regions, the use of coastal wind

data increases coverage on the sea surface around coastal regions.

## 3. Verification results

Two observing system experiments (OSEs) were performed over the periods from June 27 to August 30 2016 and from December 11 2016 to January 15 2017 to investigate the effects of ASCAT OVW data assimilation into the JMA mesoscale NWP system. One experiment (referred to here as CNTL) involved the use of OVWs from the ASCAT 25-km product, and the other (TEST) assimilated those of the ASCAT coastal product. CNTL had the same configuration as the JMA operational system, and TEST was identical to CNTL except for the ASCAT OVWs. Precipitation scores for three-hour cumulative precipitation forecasting against Radar/Raingauge-Analyzed Precipitation were improved in TEST. The bias score improved slightly for light rain, and the threat score increased. These improvements were confirmed by both summer and winter season experiments, and were remarkable for early forecast lead times. Typhoon position forecast skill was also improved, as shown in Figure 2. Figure 3 shows the example of Typhoon Mindulle in 2016. The speed of northward movement was

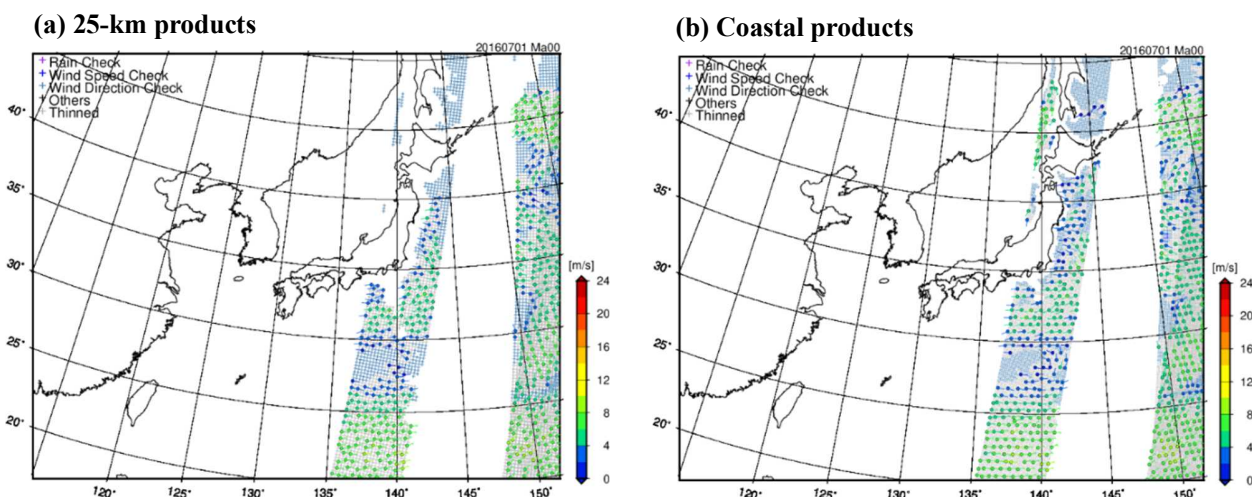


Figure 1. OVWs of (a) 25-km products and (b) coastal products in 00 UTC mesoscale analysis on July 1st 2016. Circles and crosses represent assimilated and rejected data, respectively. Colors represent wind speed for the circles and reasons for rejection (as indicated in the top left of the panels) for the crosses.

increased, and the predicted track was close to the best track from the Regional Specialized Meteorological Center (RSMC) Tokyo.

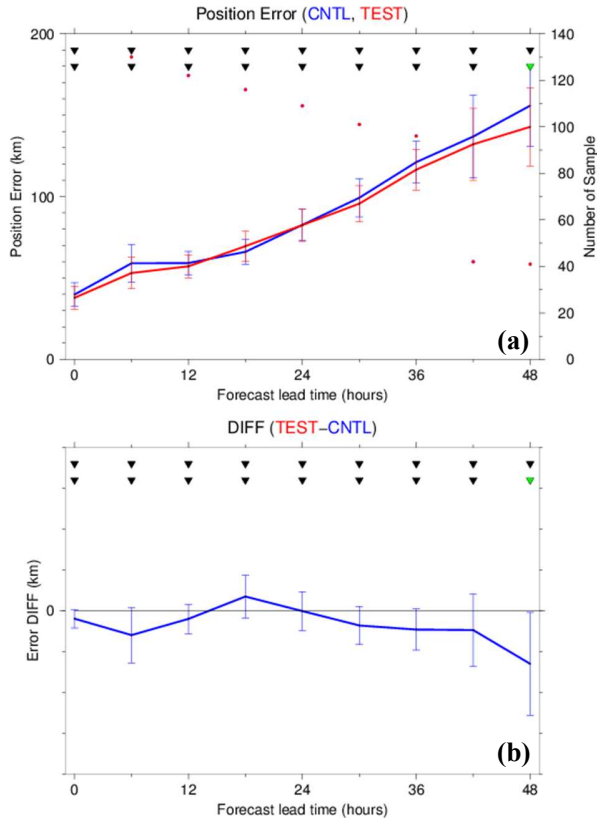


Figure 2. (a) Average typhoon track forecast errors for 8 typhoons in summer 2016. The red and blue lines represent positional errors in TEST and CNTL, respectively. Red dots indicate the number of cases included in the statistics. Forecasts were verified against best-track data from RSMC Tokyo. (b) Difference in typhoon position errors between TEST and CNTL. Negative values indicate error reductions, and error bars represent a 95% confidence interval. The triangles at the top indicate statistical significance differences, with green indicating significance.

#### 4. Summary

The use of ASCAT coastal wind data increased the spatial coverage of OVWs on the sea surface around coastal regions, and OSEs showed improved precipitation scores and typhoon track prediction. Based on these results, JMA began assimilation of ASCAT coastal products into its mesoscale NWP system on March 26 2019.

#### References

- Moriya, M., 2016: Operational use of ASCAT ocean vector wind data in JMA's mesoscale NWP system. *CAS/JSC WGNE Res. Activ. Atmos. Oceanic Modell.*, 46, 01.23-01.24
- Takahashi, M., 2010: Operational use of Metop-A/ASCAT winds in the JMA global data assimilation system. *CAS/JSC WGNE Res. Activ. Atmos. Oceanic Modell.*, 40, 01.39-01.40
- Verhoef, A., M. Portabella and A. Stoffelen, High-resolution ASCAT scatterometer winds near the coast, *IEEE Transactions on Geoscience and Remote Sensing*, 2012, 50, 7, 2481-2487

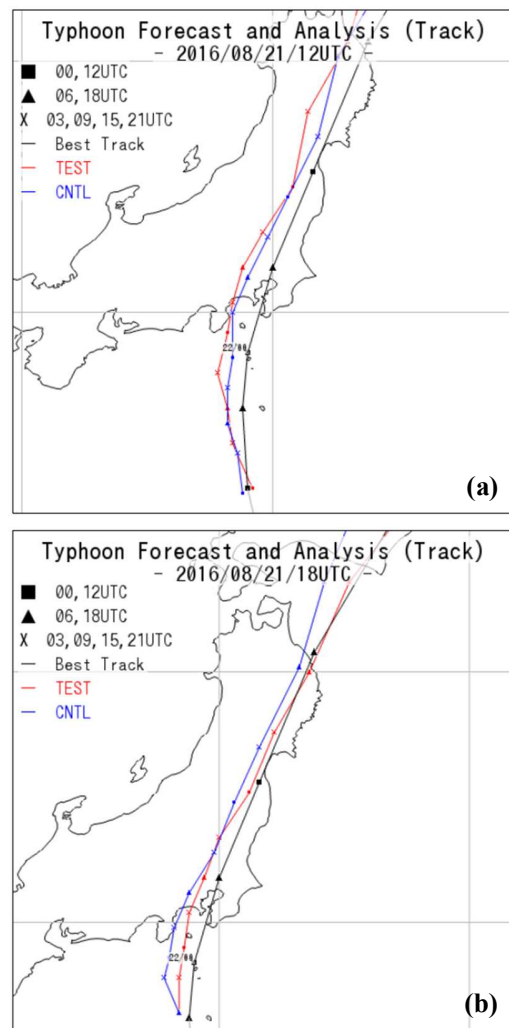


Figure 3. Track forecasts for Typhoon Mindulle at the initial times of (a) 12 UTC and (b) 18 UTC on August 21st 2016. The red and blue lines represent track predictions in TEST and CNTL, respectively, and the black lines show the best track from RSMC Tokyo.

# Evaluation of GOES-16 Clear-sky Radiance Data and Preliminary Assimilation Results at NCEP

Haixia Liu<sup>1,2</sup>, Andrew Collard<sup>1,2</sup>, John Derber<sup>3</sup>, Sharon Nebuda<sup>4</sup> and James Jung<sup>4</sup>  
1. *IMSG, Rockville, MD, U.S.A.* 2. *NCEP/EMC, College Park, MD, U.S.A.*  
3. *NCEP/EMC Retired, U.S.A.* 4. *CIMSS, University of Wisconsin*  
Email: [Haixia.Liu@noaa.gov](mailto:Haixia.Liu@noaa.gov)

## 1. ABI\_G16 CSR Data

GOES-16 is the first of the GOES-R series of geostationary weather satellites. It became operational on December 18, 2017 – replacing GOES-13 in the GOES-East position centered on the Americas. It provides high temporal and spatial resolution imagery of the Earth through 16 spectral bands at visible and infrared wavelengths, using its Advanced Baseline Imager (ABI). The numerical weather prediction (NWP) community has an interest in using radiances from the water vapor infrared channels. Due to the extremely large data volume at its original pixel level, the Clear-Sky Radiance (CSR) product has been developed at the University of Wisconsin from the 2 km pixels for the infrared channels 7-16. The baseline cloud mask is used to identify clear and cloudy pixels in a 15x15 processing box, then the brightness temperatures (BTs) from the clear pixels are averaged within the processing box. Meanwhile, the percentage of clear pixels and the standard deviation of the BTs from the clear pixels within the processing box are reported as well. These two parameters can be very helpful during the thinning process.

## 2. Evaluation of the CSR Data and Additional Cloud Detection

The ABI\_G16 CSR data quality has been evaluated at the National Centers for Environmental Prediction (NCEP) through studying the statistical characteristics of the CSR data, compared with the simulated model equivalence (OmF) using the operational Global Forecast System (GFS) model. Results have been fed back to the CSR algorithm developers. Several versions of the CSR data have been tested at NCEP/EMC. The most important change during this CSR algorithm development is the cloud mask update from the baseline cloud mask to the so-called enterprise channel dependent cloud mask. A comparison of the OmF statistics from both the baseline and enterprise cloud mask CSRs is shown in Fig. 1 for the window channel. The OmF horizontal maps in Figs. 1 (a) and (b) clearly demonstrate that the enterprise CSR removes more cloudy pixels than does the baseline CSR. Thus, both the OmF bias and standard deviation decrease significantly as shown in the histogram plot of the OmF (Fig. 1c). However, since to the enterprise version of the CSR will not be available in real time for use anytime soon, in order to operationally assimilate the CSR data in real time we have to stay with the baseline CSR. Additional cloud detections need to be performed to remove cloud contaminated data before the assimilation is done. Data from the low peaking water vapor and surface channels are excluded if the clear-sky percentage is smaller than 0.98 or the BT standard deviation from the clear pixels within the processing box is larger than 0.5k. Second, since Channel 14 is more transparent than Channel 15 under clear-sky conditions, opaque clouds can generate smaller BT differences between these two channels than the BT differences from the simulated model equivalences. Fig. 2 shows the OmF from the baseline CSR before and after the above-mentioned additional cloud tests are applied to the window channel. These additional tests remove cloud contaminated data efficiently.

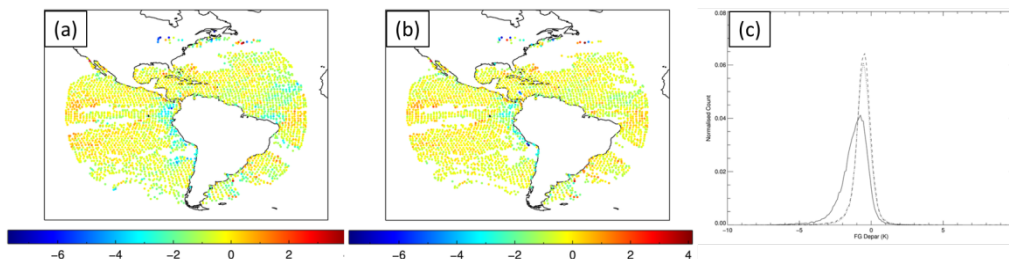


**Figure 1.** (a) is the BT differences between the baseline CSR data and the simulated model equivalences (OmF) for the window channel. (b) is the same as (a) but for the enterprise CSR data. (c) is the normalized histogram plot of the OmF from the baseline CSR in solid and the enterprise CSR in dashed and dotted lines.

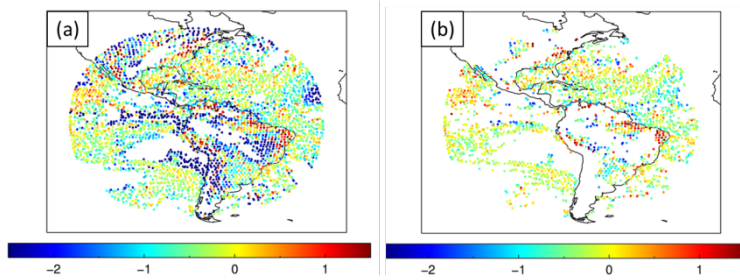


**Figure 2.** (a) and (b) are the baseline CSR OmF for the window channel before and after the two cloud tests are applied.

### 3. Preliminary CSR Assimilation Experiments and Results

The impact of the baseline CSR product has been tested in our operational GFS Data Assimilation System (GDAS) utilizing the GSI hybrid 4D<sub>En</sub>Var. Two parallel experiments were conducted with the operational configuration at a reduced resolution of T670 for the deterministic component and at T254 resolution for the 80 ensemble members. The experiments cover the period from September 22 through November 8, 2018, with the ABI\_G16 CSR data being monitored in the control and actively assimilated in the experiment. Only the three water vapor channels (Channels 8-10) are used over both water and land. Observation errors assigned are 2.4, 2.2 and 2.0 kelvin, respectively. Adaptive bias correction is initiated with zero values. The first week of the experiment is used as the bias correction spin-up period and is excluded from the verification. Fig. 3 shows the normalized OmF histograms of the three water vapor channels before and after bias correction. It appears that Channel 9 has the largest bias, and the lowest water vapor channel, 10, has little bias. The large bias for Channel 9 probably results from errors in the spectral response function or from the process of generating the CRTM coefficients (Emily Liu, personal communication). However, all three channels show good Gaussian shapes in terms of OmF after the bias correction. These preliminary assimilation experiments show neutral impact from the ABI\_G16 CSR data. In the future, the ABI\_G16 CSR data will be tested together with the SEVIRI CSR from both MSG08 and MSG11 and the AHI CSR from Himawari to have a better global coverage from geostationary instruments.

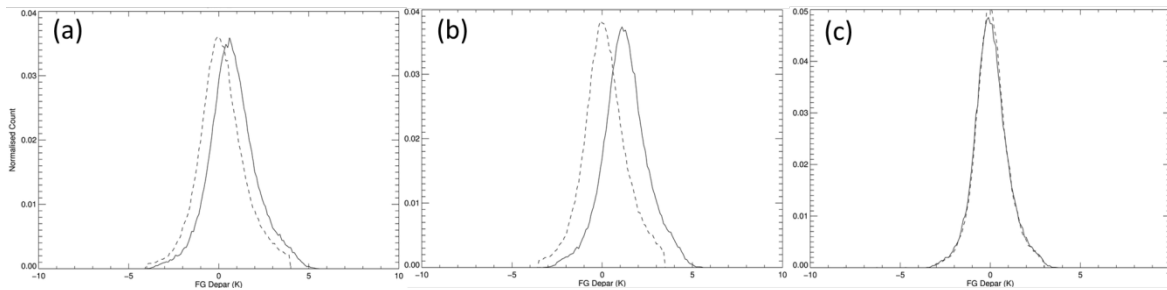


**Figure 3.** (a) is the normalized histogram plot of the OmF for the channel 8. The solid and dashed curves are before and after the bias correction. (b) and (c) are the same as (a) but for the channels 9 and 10, respectively.

### Acknowledgments

Thanks to Qiang Zhao, Peter Keehn and Tom King at NESDIS and Yangrong Lin at NCEP/EMC for supporting the ABI\_G16 CSR real-time BUFR data.

# Operational Use of NOAA-20 ATMS and CrIS Radiance Data in JMA's Global NWP System

Hidehiko Murata and Norio Kamekawa

Numerical Prediction Division, Japan Meteorological Agency

E-mail: [hidehiko.murata@met.kishou.go.jp](mailto:hidehiko.murata@met.kishou.go.jp)

## 1. Introduction

The Japan Meteorological Agency (JMA) has assimilated radiance data from the Advanced Technology Microwave Sounder (ATMS) and the Cross-track Infrared Sounder (CrIS) onboard the Suomi National Polar-orbiting Partnership (Suomi-NPP) since 29 March 2017 in its global Numerical Weather Prediction (NWP) system. In addition to Suomi-NPP data, JMA also began to assimilate data from the same instruments onboard the NOAA-20 successor satellite on 5 March 2019 into the global NWP system. This report outlines the impacts of the added data on the system.

## 2. Methodology

The ATMS instrument is a microwave sounder with 22 channels, including temperature and humidity sounding channels. Quality control (QC) and error handling for the assimilation of NOAA-20/ATMS radiance data, such as channel selection, thinning distance, observation errors, rain/cloud detection and bias correction (static scan bias correction and variational bias correction) follow those implemented for Suomi-NPP/ATMS data assimilation (Hirahara et al. 2017). Currently, tropospheric temperature-sounding channels (6 – 9) and humidity-sounding channels (18 – 22) are assimilated.

The CrIS instrument is a hyperspectral infrared sounder with a total of 2,211 channels in full spectral resolution (FSR) mode. QC and error handling for the assimilation of NOAA-20/CrIS radiance data also follow those for Suomi-NPP/CrIS (Kamekawa and Kazumori 2017). Currently, 27 channels for temperature-sounding are assimilated. The channels are selected from the CO<sub>2</sub> absorption band in the long-wave IR band (LWIR) included in the disseminated 431 channel dataset.

## 3. Impacts on the global NWP system

Observing system experiments covering periods in each of boreal summer 2018 and winter 2019 were performed to evaluate the impacts of NOAA-20 instruments on the NWP system. The standard deviations of the first-guess departure (i.e., the difference between observed and calculated brightness temperature), which are used as an indicator of data quality, were similar to or smaller than those of Suomi-NPP. Against baseline experiments in which the focusing radiance data of both satellites were not assimilated, the impacts of Suomi-NPP and NOAA-20 on first-guess and forecast-field data were similar.

A TEST assimilation experiment with the addition of NOAA-20/ATMS and CrIS data was performed. Experiments for individual instruments were also performed to determine their specific contributions. Figure 1 shows changes in the standard deviation of the first-guess departure of the AMSU-A and MHS microwave sounders normalized to those of the CNTL experiment (without NOAA-20). The lines show the results of assimilating NOAA-20 ATMS (red), CrIS (green) and both instruments (blue). The improvements observed with the temperature sounding channels (AMSU-A/ch4-8) and humidity sounding channels (MHS) are mainly attributable to the assimilation of ATMS data, and those observed with the stratospheric temperature sounding channels (AMSU-A/ch9-14) are attributable to the assimilation

of CrIS data.

Figure 2 shows the zonal mean of the improvement rate of geopotential height forecast data resulting from the assimilation of NOAA-20/ATMS and CrIS data in the TEST experiment relative to the CNTL experiment. Improvements in geopotential height forecast data, especially for the mid-latitudes, were observed in the TEST experiment in the boreal summer experiment, and were also seen in the boreal winter experiment (not shown).

#### 4. Summary

JMA began to assimilate data from the ATMS and CrIS onboard NOAA-20 into its global NWP system in addition to those of Suomi-NPP on 5 March 2019. NOAA-20 data quality is similar to or better than that of Suomi-NPP, and the additional use of NOAA-20 data improved the first-guess and forecast fields.

#### References

- Hirahara, Y., T. Egawa and M. Kazumori, 2017: Operational use of Suomi NPP ATMS radiance data in JMA's global NWP system. CAS/JSC WGNE Research Activities in Atmospheric and Oceanic Modelling, Rep., 47, 1 – 13.
- Kamekawa, N. and M. Kazumori, 2017: Assimilation of Suomi NPP/CrIS radiance data into JMA's global NWP system. CAS/JSC WGNE Research Activities in Atmospheric and Oceanic Modelling, Rep., 47, 1 – 17.

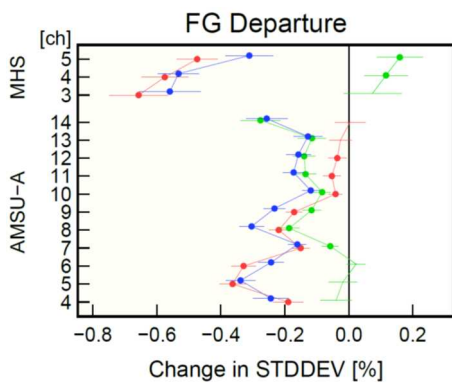


Figure 1. Normalized changes in the standard deviation (STDDEV) of the first-guess departure of microwave sounders AMSU-A and MHS resulting from assimilation of NOAA-20 ATMS (red), CrIS (green) and both (blue). Negative values indicate improvement, error bars represent a 95% confidence interval, and dots represent statistically significant changes. The validation period is from 1st August to 31st October 2018 (92 days).

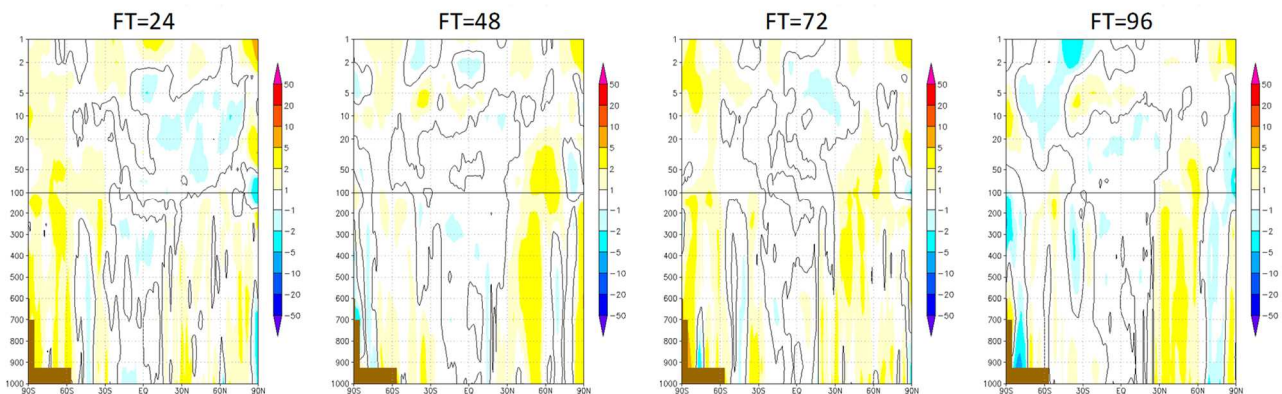


Figure 2. Zonal mean of the relative improvement rate [%] in the TEST experiment (with NOAA-20/ATMS and CrIS) relative to the CNTL experiment (without NOAA-20/ATMS and CrIS) in RMS error against own analysis of each experiment for geopotential height forecast. Warm colors indicate forecast error reduction. The validation period is from 1st August to 31st October 2018 (92 days).

# Operational use of surface-sensitive clear-sky radiance data in JMA's mesoscale NWP system

Izumi Okabe

Numerical Prediction Division, Japan Meteorological Agency

E-mail: i-okabe@met.kishou.go.jp

## 1. Introduction

The Japan Meteorological Agency (JMA) began to use Himawari-8 surface-sensitive band 9 and 10 (6.9 and 7.3  $\mu\text{m}$ ) clear-sky radiance (CSR) data in its mesoscale NWP system on March 26 2019 in addition to band 8 (6.2  $\mu\text{m}$ ) CSR data (Kazumori 2018). Experiments indicated that this assimilation with a new radiative transfer (RT) calculation method for JMA's global NWP system also had positive impacts on water vapor (WV) field first-guess (FG) and precipitation forecasting scores in the mesoscale NWP system. The results are reported here.

## 2. Methodology

The new RT calculation method is the same as that of the global NWP system (Okabe 2019). The land surface emissivity atlas of Wisconsin University (Borbas and Ruston 2010) and retrieved land surface temperatures from window channel (10.8  $\mu\text{m}$ ; band 13) CSR observation data are used in the calculation.

## 3. Assimilation experiment

The control experiment performed (referred to here as CNTL) had the same configuration as the operational JMA mesoscale NWP system as of October 2018. The test experiment (TEST) was as per CNTL, but surface-sensitive CSRs from Himawari-8 (band 9 and 10) were additionally assimilated. The experiment periods were from June 22 to July 31 2017 (referred to as summer) and from December 6 2017 to January 15 2018 (referred to as winter).

## 4. Impacts on the NWP system

Figure 1 shows normalized changes in the standard deviation (STD) of the FG departure for microwave humidity sounder (MHS) and microwave imager data, which contain information on WV in the troposphere. The decreases indicate the improvement of fittings between FG and other observations. Figures 2 (a) and (b) show the data counts of Himawari-8 band 9 CSR used in the TEST experiment. Figures 2 (c) and (d) show differences in the FG departure STD for MHS between TEST and

CNTL. The decreases observed (plotted in blue) were seen in particular over areas where counts of newly assimilated data were relatively large (as indicated by red circles). These results imply that assimilation of surface-sensitive CSRs contributes to reducing WV field errors in mesoscale model (MSM) FG data.

Figure 3 shows threat scores and bias scores for three-hour cumulative precipitation forecasts. Reductions of precipitation forecasting underestimation in the summer experiment and overestimation in the winter experiment are observed, and slight improvements are seen in threat scores.

## 5. Summary

JMA began to assimilate surface-sensitive CSRs from Himawari-8 (bands 9 and 10) in the mesoscale NWP system on March 26 2019, and the new RT calculation method used in JMA's global NWP system was applied. Positive impacts from these CSRs on WV field accuracy of the first guess in the MSM were shown in an assimilation experiment, which also revealed improved precipitation forecasting scores.

## References

- Borbas, E. E. and Ruston, B. C. (2010). The RTTOV UWiremis IR land surface emissivity module, AS Mission Report NWPSAF-MO-VS-042, EUMETSAT Numerical Weather Prediction Satellite Applications Facility, 24pp.
- Kazumori, M., 2018: Assimilation of Himawari-8 Clear Sky Radiance data in JMA's global and mesoscale NWP systems. *J. Meteor. Soc. Japan*, 96B, 173-192.
- Okabe, I., 2019: Operational use of surface-sensitive Clear-Sky Radiance (CSR) data in JMA's Global NWP System. CAS/JSC WGNE Research Activities in Atmospheric and Oceanic Modelling, Rep. 49, 1.15-1.16.

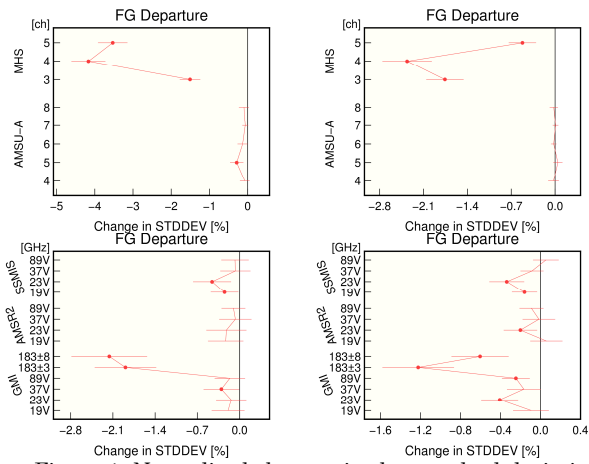


Figure 1. Normalized changes in the standard deviation (STDDEV) of first-guess departures for microwave sounding data for each channel [ch] (top) and microwave imager data for each channel's frequency [GHz] (bottom). "V" means the polarization as vertical. The validation periods are from June 27 to July 31 2017 (right) and from December 11 2017 to January 15 2018 (left).

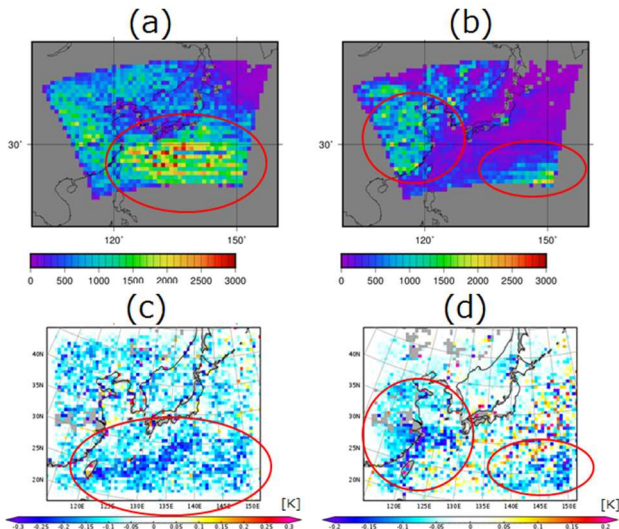


Figure 2. Counts of Himawari-8 band 9 CSR data used in the TEST experiment of the summer period (a) and the winter period (b), and normalized changes in the standard deviation of first-guess departures for MHS (channel 4) between the TEST and CNTL experiments for the summer period (c) and the winter period (d)

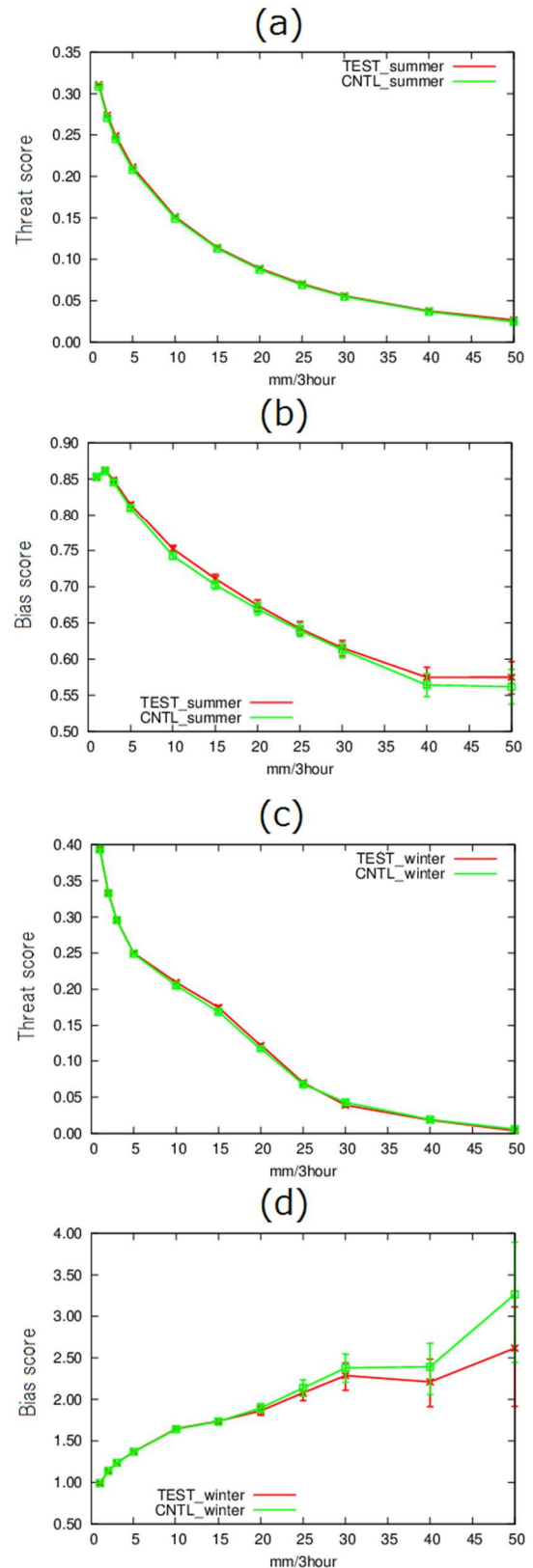


Figure 3. Threat scores (a), (c) and bias scores (b), (d) for three-hour cumulative precipitation forecasts against Radar/Raingauge-Analyzed Precipitation data during the summer experiment period (a), (b) and the winter experiment period (c), (d). Green lines are for CNTL and red lines are for TEST. Error bars represent 95% confidence intervals.

# Operational use of surface-sensitive clear-sky radiance data in JMA's global NWP system

Izumi Okabe

Numerical Prediction Division, Japan Meteorological Agency

E-mail: i-okabe@met.kishou.go.jp

## 1. Introduction

Clear-sky radiance (CSR) data from geostationary satellites contain information on water vapor (WV) amounts in the upper troposphere. The usage of surface-sensitive (WV band; 6.9 and 7.3  $\mu\text{m}$ ) CSR data from Himawari-8 was previously limited over ocean areas in the Japan Meteorological Agency's (JMA's) global NWP system (Kazumori 2018) because accurate land surface temperature and emissivity information is required for assimilation. Against this background, JMA developed a new methodology for radiative transfer (RT) calculation using retrieved land surface temperature data. Assimilation experiments performed with this methodology indicated that surface-sensitive CSRs from Himawari-8 and Meteosat Second Generation (MSG) data for areas over land had positive impacts on WV field accuracy in first-guess (FG) and forecasting scores from JMA's global spectral model (GSM). The results of these experiments are reported here.

## 2. Methodology

To improve RT calculation accuracy, JMA now uses the atlas of Wisconsin University (Borbas and Ruston 2010) for land surface emissivity data rather than a constant value (0.90) and land surface temperatures from Himawari-8's band-13 window channel (10.8  $\mu\text{m}$ ) CSRs rather than FG surface temperature data from the GSM. These CSR observation data and FG atmospheric profiles are leveraged in RT calculation to determine land surface temperatures, which are in turn used in RT calculation to derive FG brightness temperatures for WV-band CSRs. Quality control (QC) is modified to rejected CSR data for altitudes exceeding 4,000 m in GSM topography, thereby eliminating the use of CSR data over the Tibet Plateau, where extremes of geographical relief cause gaps between actual altitudes and those used in the GSM. These gaps affect the accuracy of RT calculation, and CSR data for areas over high mountains contain less WV information than those for areas over low plains

and oceans, since there is less WV at such high altitudes. The time interval for assimilation of Meteosat and GOES CSR data was also changed from two hours to an hour in addition to the adoption of Himawari-8 CSR data usage.

## 3. Assimilation experiment

The control experiment (referred to here as CNTL) had the same configuration as the operational JMA global NWP system as of June 2018. Surface-sensitive CSRs from Himawari-8 and MSGs were assimilated, and QC for CSR data at high altitudes and the periodicity change were added to the test experiment (referred to as TEST). The experiments covered periods of around four months from June 10 to October 11 2017 and from November 10 2017 to March 11 2018.

## 4. Impacts on the NWP system

Figure 1 shows normalized changes in the standard deviation (STD) of FG departure for microwave humidity sounder (MHS) data and radiosonde observation data on relative humidity. The reduced values indicate an improvement in correspondence between FG and other observations. Figure 2 shows differences in the FG departure's STD for MHS data between TEST and CNTL. Decreases (plotted in blue) in STD were observed over land areas (e.g., Australia and Africa). As these observations contain information on WV in the troposphere, the results suggest a positive impact from surface-sensitive CSR assimilation over land on WV field accuracy for FGs in the troposphere. Forecasting scores in the short range were improved in the fields of humidity, temperature and wind speed (Figures 3 and 4). The altitude of forecasting improvement was that in which correspondence between FG and radiosonde observations was enhanced, as shown in Figure 1.

## 5. Summary

JMA began assimilating surface-sensitive CSR data from Himawari-8 for areas over land and MSG data for areas over land and oceans on October 18 2018. A new RT calculation method

involving the use of data from the Wisconsin University land surface emissivity atlas and land surface temperatures retrieved from window-channel CSR observation data was developed for assimilation of surface-sensitive CSRs. At the same time, the quality control was modified to remove CSR data from high-altitude areas. The time interval for the assimilation of Meteosat and GOES CSRs was changed from two hours to an hour, and positive impacts from surface-sensitive CSR assimilation on the WV field of the FG were found. Improved short-range forecast scores were also observed for specific humidity, temperature, wind speed and geopotential height fields in the assimilation experiment.

### References

- Borbas, E. E. and Ruston, B. C. (2010). The RTTOV UWiremis IR land surface emissivity module, AS Mission Report NWPSAF-MO-VS-042, EUMETSAT Numerical Weather Prediction Satellite Applications Facility, 24pp.
- Kazumori, M., 2018: Assimilation of Himawari-8 Clear Sky Radiance data in JMA's global and mesoscale NWP systems. *J. Meteor. Soc. Japan*, 96B, 173-192.

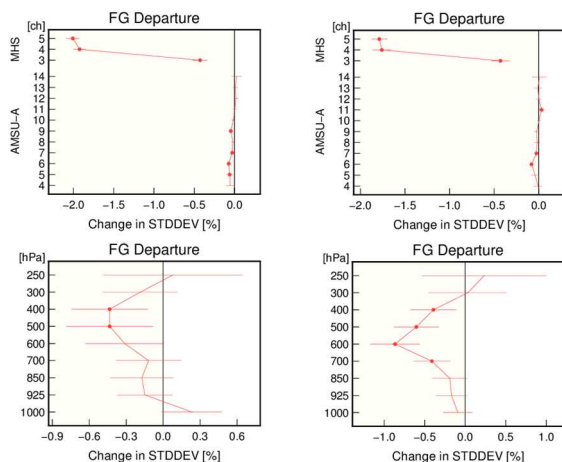


Figure 1. Normalized changes in the standard deviation (STDDEV) of first-guess departures for microwave sounding data for each channel number [ch] (top) and radiosonde observation data for relative humidity for each pressure height (bottom). The validation periods are from June 21 to October 11 2017 (right) and from November 21 2017 to March 11 2018 (left).

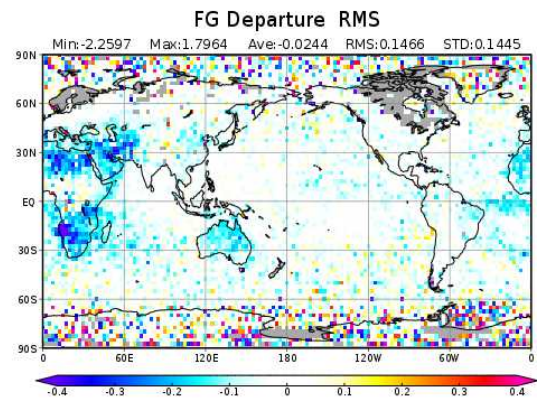


Figure 2. Normalized changes in the standard deviation of first-guess departures for MHS (channel 4). The validation period is from June 21 to October 11 2017.

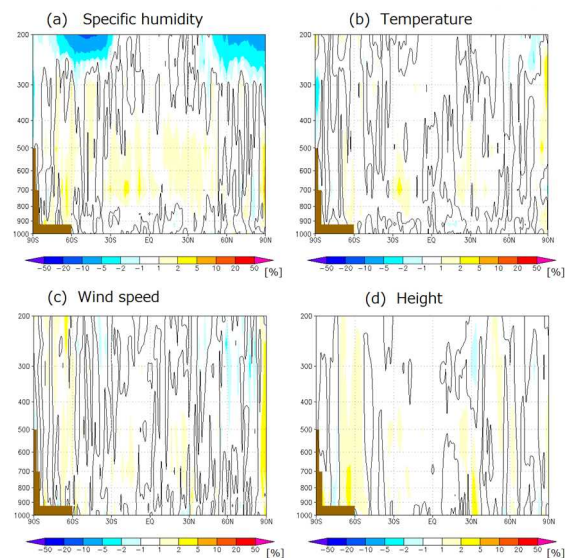


Figure 3. Relative improvement of root mean square error of 24-hour forecasts for (a) specific humidity, (b) temperature, (c) wind speed and (d) height. Forecasts of only 12 UTC initials were counted, and ECMWF analysis was used in validation. The validation period is from July 1 to September 30 2017.

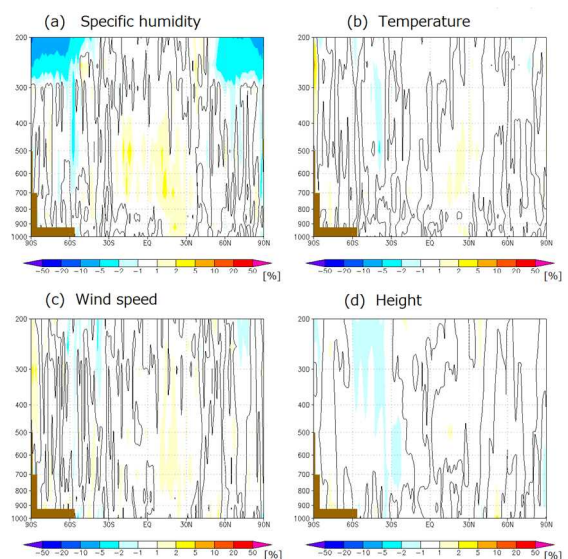


Figure 4. As per Fig. 3, but with a validation period from December 1 2017 to February 28 2018.

# Bias Correction of Aircraft Temperature Data in JMA's Mesoscale Data Assimilation System

Yukinari Ota

Numerical Prediction Division, Japan Meteorological Agency

e-mail: y.otta@met.kishou.go.jp

## 1. Introduction

Ballish and Kumar (2008) reported that aircraft temperature data exhibit various biases depending on aircraft type, and exhibit statistically higher values than similar data from radiosonde observation.

Against this background, correction for aircraft temperature bias was introduced to the JMA global data assimilation system (GA) in November 2009 (Sako 2010) and to the mesoscale data assimilation system (MA) in March 2019.

## 2. Bias correction methodology

Estimated temperature biases in the GA system are applied to bias correction for aircraft temperature in the MA system. The bias estimation method for the GA system is based on monthly statistics of first-guess (FG) departures for individual aircraft tail numbers and flight levels over the previous month (Sako 2010).

## 3. Impacts of bias correction

Observing system experiments on the mesoscale NWP system were performed over a month in summer 2018. Figure 1 compares the resulting FG departure fits to aircraft temperature data between the two experiments without and with bias correction (noBC and BC, respectively). It can be seen that aircraft temperature bias correction significantly reduces biases and standard deviations of FG departure. Figure 2 shows FG departure fits to radiosonde temperature data. It can be inferred that the use of bias-corrected aircraft temperature data leads to bias reduction in radiosonde temperature data from over 300 hPa and standard deviations in many layers, which improves the FG against radiosonde temperature data. In the area of forecast improvement, Figure 3 shows verification of mean errors and root mean square errors against radiosonde temperature data in 12-hour forecasting during the experiment period. A positive impact is generally seen above 300 hPa, with reduced positive temperature bias and root mean square errors.

## 4. Summary

Aircraft temperature bias correction is generally required in data assimilation systems to reduce positive biases and root mean square errors above 300 hPa. Based on the related impacts, such correction was introduced to JMA's operational mesoscale data assimilation system in March 2019.

## References

- Ballish, B. A., and K. Kumar, 2008: Systematic differences in aircraft and radiosonde temperatures. *Bull. Amer. Meteor. Soc.*, **89**, 1689–1708.
- Sako, H.: 2010: Assimilation of aircraft temperature data in the JMA global 4D-Var data assimilation system, CAS/JSC WGNE Research Activities in Atmospheric and Oceanic Modelling, **40**, 1 – 33.

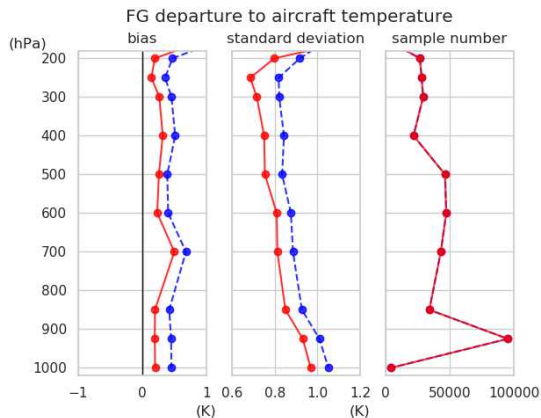


Figure 1. Biases (right), standard deviations (center) and sample numbers (left) of fits of the first-guess departure to aircraft temperature data in the experiment. Blue: noBC; red: BC.

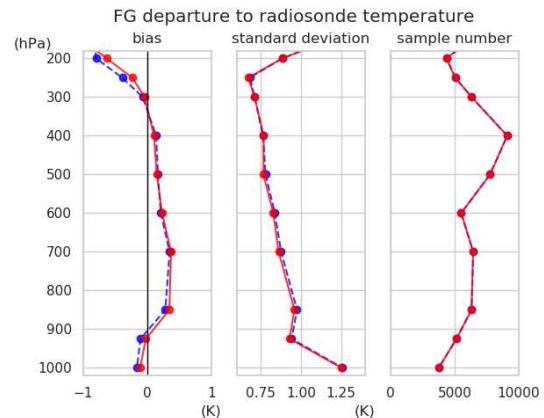


Figure 2. As per Fig. 1, but for radiosonde temperature data.

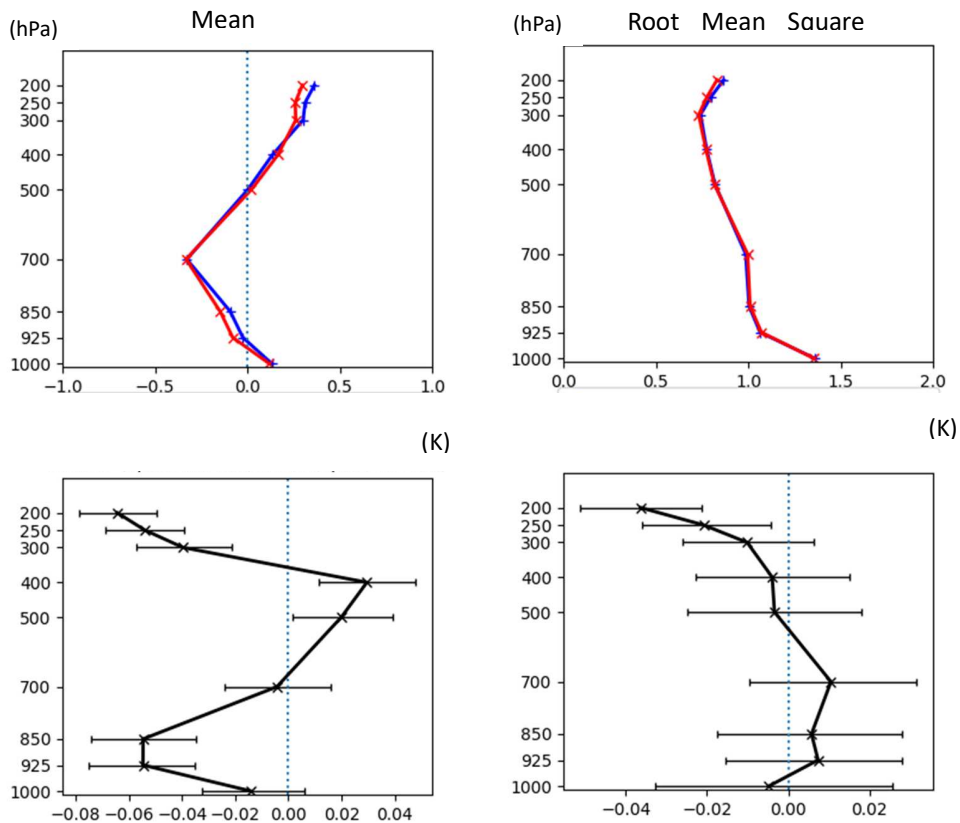


Figure 3. Fits to radiosonde data for 12-hour forecasting of temperature in the experiments. (a) Vertical profile of mean error (ME), (b) BC-noBC of ME, (c) vertical profile of root mean square error (RMSE), (d) ratio of RMSE change  $((BC-noBC)/|noBC|)$ . The red and blue lines represent BC and noBC, respectively, and error bars represent 95% confidence intervals.

# Multigrid Beta function approach for modeling of background error covariances in the Real Time Mesoscale Analysis

R. James Purser and Miodrag Rancic

*IM Systems Group at NOAA/NCEP/EMC, College Park, MD 20740, USA*

*Email: jim.purser@noaa.gov*

The Real Time Mesoscale Analysis (RTMA) and UnRestricted Mesoscale Analysis (URMA) projects provide hourly and sub-hourly analyses of surface variables, cloud cover and precipitation on the National Weather Service's National Digital Forecast Database grid. They are used for situational awareness, current conditions for transportation customers, verification of forecasts and as the reference for the bias correction in the National Blend of Models.

One major development underway is a fully three-dimensional "3D RTMA" system, which should replace the current two-dimensional (2D) system within the next year or two. It will provide 3D analyses at very high horizontal resolutions (~1.25 km) issued at very frequent time intervals (~15 min). One key prerequisite for the success of such an enterprise is a vastly improved efficiency in producing those analyses. The new approach to modeling of background error covariances, which will be discussed here, is one of the key components for the success of that effort.

Recursive filters (Purser et al. 2003a, b) represent efficient and very good approximations to the Gaussian components of which each univariate covariance operator is composed, and they accommodate spatial inhomogeneity and local anisotropy of analyzed field increments. On the down side, a recursive filter, being inherently sequential and with infinite support, is very difficult to successfully parallelize. Also, it is not easily able to describe covariances across various scales, or to take into account cross-correlations between different variables, or to provide the negative side-lobes which realistic covariance often possess.

Our alternative to recursive filters is based on the Beta distribution filters. The "radial" version of the Beta filter is defined, in any number of dimensions, as having the smoothing kernel:

$$\beta(\mathbf{r}) = \begin{cases} (1 - \rho)^p, & \rho \leq 1 \\ 0 & , \rho > 1 \end{cases} ,$$

where  $p$  is a small positive integer exponent and, in the isotropic case,

$$\rho = \frac{1}{s^2} \mathbf{r} \cdot \mathbf{r}^T .$$

Here,  $s$  is a radial scale and  $\mathbf{r}$  the displacement vector, e.g., in 2D,  $\mathbf{r} = (x, y)$ . Such a  $\beta$  function also has a quasi-Gaussian shape, but with a finite support. In an anisotropic generalization  $s^2$  is replaced by a symmetric, positive-definite "aspect tensor", used as its matrix inverse  $\mathbf{A}^{-1}$ , so that:

$$\rho = \mathbf{r} \mathbf{A}^{-1} \mathbf{r}^T .$$

A larger exponent  $p$  implies a more Gaussian shape, but also a narrower one. The Beta filter is further used at a hierarchy of different scales, suitably weighted and combined in a multigrid

scheme, in order to achieve a larger coverage and potentially a more versatile synthesis of anisotropic covariances, and allowing a greater control over the shape. Each successive “generation” of the multi-grid hierarchy, is characterised by successive factors of two in grid spacing and scale going from fine to coarse. Each generation is given separate weights, which signify the effect of these scales in the final solution.

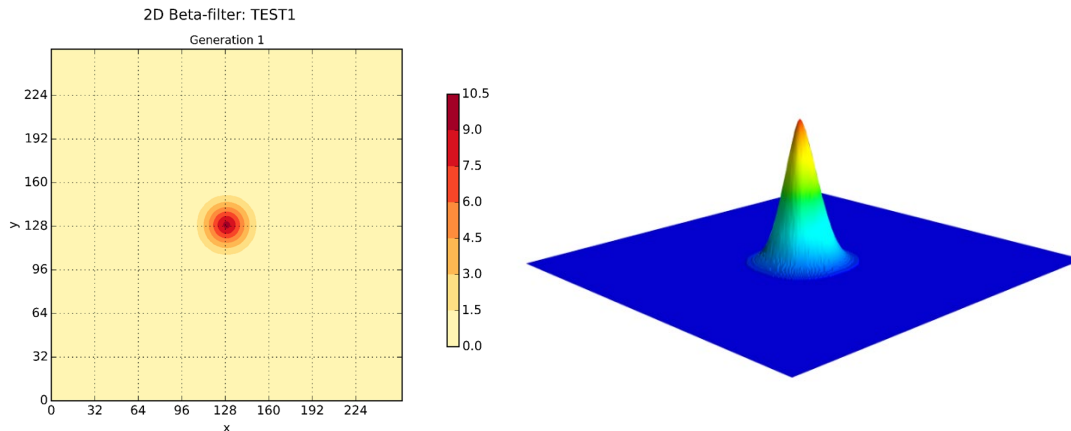


Fig. 1. Appearance of delta function impulse after application of the multigrid Beta filter.

A very efficient, “line” version of the filter is also being developed which, in small numbers of sequential combinations, can fill out the higher dimensions of a covariance operator (up to four dimensions), to eventually supersede the less efficient radial versions of the corresponding filter in final applications. Among other novelties, we are planning to introduce a new efficient method for normalization of covariances and a neural network approach for determining scale weights. The versatility of the approach will also allow us to introduce and experiment with the cross-covariances in the definition of the background error covariance by replacing scalar weights acting on variables separately, by self-adjoint differential operators acting on several variables together. Other plans include application of this technique on the cubed-sphere, which will enable running data assimilation directly on that geometry, and an application within the new Joint Effort for Data assimilation Integration (JEDI) based on object-oriented principles.

## References

- Purser, R. J., W.-S. Wu, D. F. Parrish, and N. M. Roberts, 2003: Numerical aspects of the application of recursive filters to variational statistical analysis. Part I: Spatially homogeneous and isotropic Gaussian covariances. *Mon. Wea. Rev.*, **131**, 1524-1535.
- Purser, R. J., W.-S. Wu, D. F. Parrish, and N. M. Roberts, 2003: Numerical aspects of the application of recursive filters to variational statistical analysis. Part II: Spatially homogeneous and anisotropic Gaussian covariances. *Mon. Wea. Rev.*, **131**, 1536-1548.

# Impact of Data Assimilation of Shipborne GNSS Data on Rainfall Forecast

Hiromu Seko, Ko Koizumi and Yoshinori Shoji

Meteorological Research Institute / Japan Meteorological Agency  
e-mail:hseko@mri-jma.go.jp

## 1. Introduction

Recently, heavy rainfalls occur almost every year in Japan. To reduce the damage caused by heavy rainfall, the accuracy of rainfall forecasts should be improved. Japan is surrounded by the sea and the most of low-level inflows that supply water vapor to heavy rainfalls originate from over the sea. Because water vapor supplied from low-level inflows affects greatly the rainfall amount, accurate water vapor data over the sea is needed to improve the heavy rainfall forecasts. The satellites provide water vapor distributions over the sea. However, the observation frequency is only a few times a day. To overcome this point, we used the GNSS data observed on the vessel (Shipborne GNSS). In this study the impact of GNSS PWV obtained by the JMA's vessel (Ryofu-maru) was investigated by using Meso-NAPEX.

## 2. Data assimilation method

The Meso-NAPEX (Numerical Analysis and Prediction EXperiment system) is a quasi-operational Data Assimilation system which enables us to make data assimilation cycle experiments(<http://jksv-pj.npd.naps.kishou.go.jp/redmine/base/projects/napex-model/wiki/NAPEX%E3%81%A8%E3%81%AF>). The grid interval of the Meso-NAPEX is 5 km. The data assimilation window is 6 hours and the observation data are assimilated every hour. As the target event for the data assimilation experiment, the precipitation system associated with the low-pressure system, which passed over Kyushu on 5<sup>th</sup> June 2017, was adopted. On June 5<sup>th</sup>, the Ryofu-maru stayed south of Kyushu, on the immediately southern side of precipitation system (windward side of low-level inflow).

We performed two experiments, in which the convective data of JMA including the satellite was assimilated by using the Meso-NAPEX (CNTL) and the PWV data of shipborne GNSS was added to the conventional data (S-GNSS). The accuracy of shipborne GNSS PWV is 3.4–5.4 mm root mean square differences against radiosonde (Shoji et al 2016). Firstly, the data assimilation period which is needed to improve the rainfall distribution was investigated by changing the start time of data assimilation. After checking the data assimilation period, the differences of water vapor during the assimilation period and the rainfall distributions of extended forecasts are investigated.

## 3. Impact of Shipborne GNSS data

The start time of data assimilation was changed from 00UTC 4<sup>th</sup> June to 00UTC 7<sup>th</sup> June with the increment of 12 hours. The rainfall distribution of the extended forecast, of which the initial

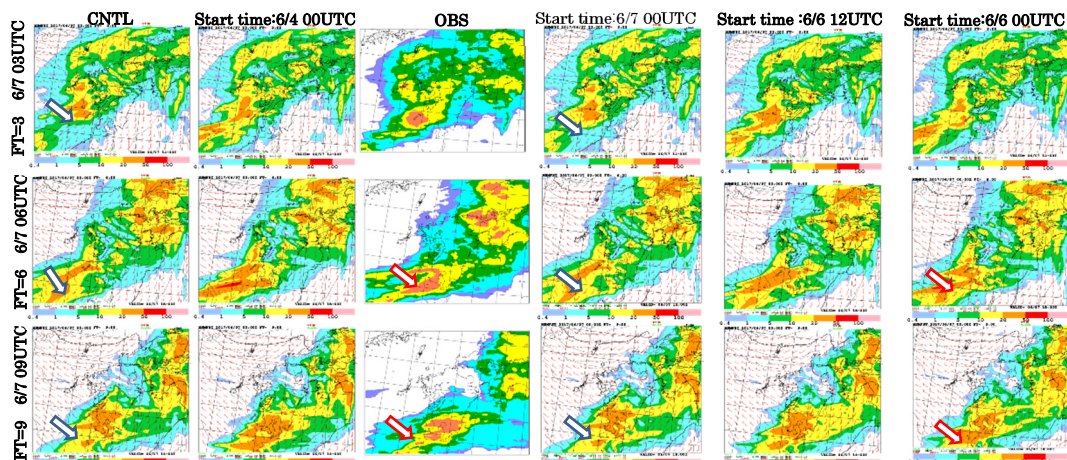


Fig. 1: The rainfall distributions of extended forecasts, of which the start time of data assimilation was changed from 00UTC 4<sup>th</sup> to 00UTC 7<sup>th</sup> June 2017. FT stands for the forecast time.

condition was produced from the analysis of 00UTC 7<sup>th</sup>, was similar to that of CNTL (Fig. 1). When the start time of data assimilation was 00UTC 6<sup>th</sup>, rainfall distribution became most similar to the observed ones. These results indicate that the impact of one GNSS data is very weak and that one day for the data assimilation was needed to increase the rainfall accuracy in this case. The start time of 00UTC 6<sup>th</sup> is adopted in the following comparisons.

The difference of T-Td at the height of 850 hPa (S-GNSS - CNTL) during the assimilation period of 00UTC 6<sup>th</sup> to 00UTC 7<sup>th</sup> is shown in Fig. 2. The T-Td around the Ryofu-maru was modified and the modified regions expanded south-southeastward with time. The region where water vapor is increased appeared at the southern side of Kyushu at 00UTC 7<sup>th</sup> (as indicated by the arrow). The comparisons of the rainfall distributions between Observation, CNTL and S-GNSS indicate that the intense rainfall regions south of Kyushu became similar to the observed ones by the assimilation of Shipborne GNSS data (indicated by arrows in Fig. 3). This assimilation result shows that Shipborne GNSS has the potential to improve rainfall forecasts through the data assimilation, even if the number of observations is small.

**References**

Shoji, Y., K. Sato, M. Yabuki and T. Tsuda, 2016: PWV Retrieval over the Ocean Using Shipborne GNSS Receivers with MADOCA Real-Time Orbits, *SOLA*, **12**, 265-271.

**Acknowledgements**

The part of this study is supported by Grant-in-Aid for Scientific Research (A) ‘A challenge to the high functionality of Tsunami observation and the continuous observation of crustal movement at sea floor using the marine GNSS buoy’.

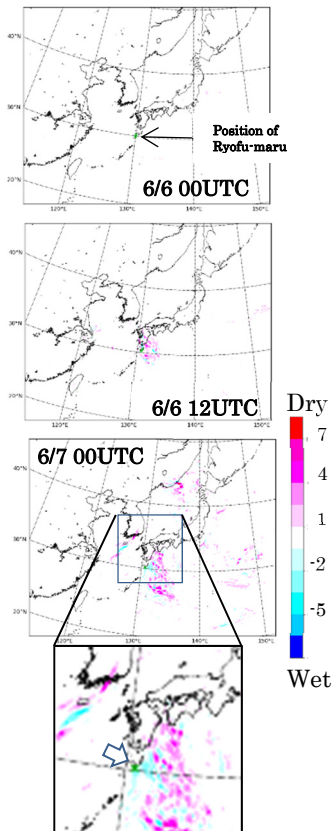


Fig. 2: Difference of analyzed T-Td fields at 850 hPa (S-GNSS -CNTL). The green crosses indicate the positions of Ryofu-maru.

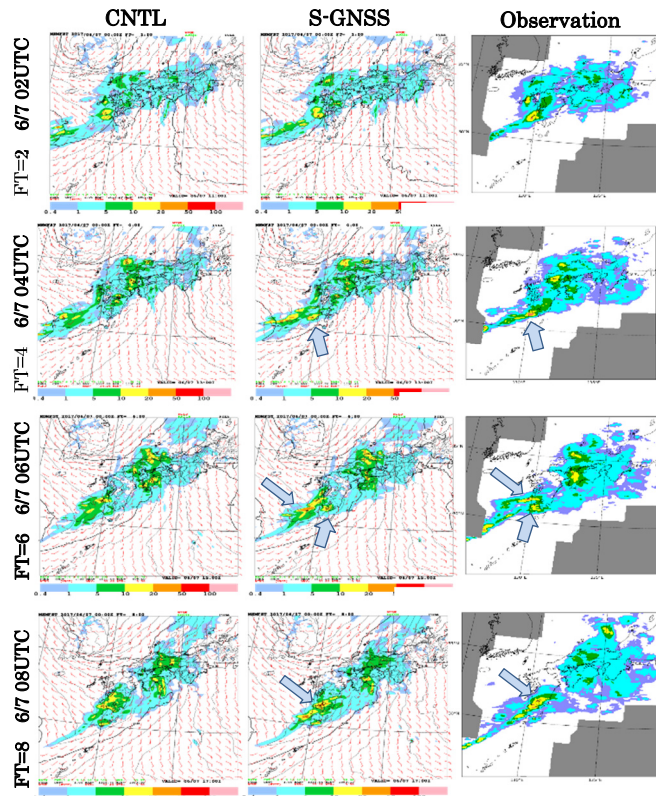


Fig. 3: Rainfall distributions predicted from the analyzed fields of 00UTC of 7<sup>th</sup> June. (left) CNTL and (center) S-GNSS, (right) Observed rainfall regions obtained by JMA's Radars and rain gauges.

# Enhanced Use of Ground-based GNSS Data in JMA's Mesoscale Data Assimilation System

Yasuhito Tani and Yukinari Ota  
Japan Meteorological Agency, Japan  
e-mail: yasuhito-tani@met.kishou.go.jp

## 1. Introduction

Based on atmospheric delays in GNSS (Global Navigation Satellite System) signals, it is possible to determine the absolute water vapor content of the atmosphere. Against this background, the Japan Meteorological Agency (JMA) uses precipitable water vapor (PWV) data from the Geospatial Information Authority of Japan's nationwide ground-based GEONET (the GNSS Earth Observation NETWORK system, which has approximately 1,300 receivers located throughout Japan; Figure 1) for its mesoscale data assimilation system (see Ishikawa (2010) for details, including JMA's usage of ground-based GNSS data). Quality control for PWV data derived from ground-based GNSS data has been improved.

## 2. Availability of GNSS PWV data

JMA previously reported that PWV data derived from ground-based GNSS data in rainy conditions (referred to as rain data) had a negative bias against the first guess in mesoscale analysis. As a result, data from areas with approximately  $\geq 1.5$  mm/hour of rainfall were rejected in quality control and not used in mesoscale analysis. However, a review based on PWV data collected since 2015 indicated that rain data exhibit no bias in any season (Figure 2). As the mesoscale model has been improved, negative biases were reduced and rain data are now considered appropriate for use with the current mesoscale data assimilation system.

## 3. Impacts of rain data

Observation system experiments for data assimilation and forecast system usage with the addition of rain data (referred to here as TEST) were performed over the period from 18 June to 23 July 2018. Figure 3 shows the resulting lower dry bias and root mean square errors for forecasting of surface specific humidity. Figure 4 shows the equitable threat score (ETS) for three-hour cumulative precipitation forecasts, and indicates

that rain data have a positive impact on high-intensity precipitation data within a six-hour forecasting range.

## 4. Summary

JMA's mesoscale data assimilation system previously rejected PWV data derived from ground-based GNSS data in rainy conditions due to negative biases against the first guess. However, such data are now considered appropriate based on a review using the latest mesoscale assimilation system. The data have positive impacts on forecasting of surface specific humidity and precipitation. Based on these impacts, PWV data in rainy conditions has been used in JMA's operational mesoscale data assimilation system since 26 March 2019.

## References

Ishikawa, Y., 2010: Data assimilation of GPS precipitable water vapor into the JMA mesoscale numerical weather prediction model. CAS/JSC WGNE Research Activities in Atmospheric and Oceanic Modelling, **40**, 01.13 – 01.14.

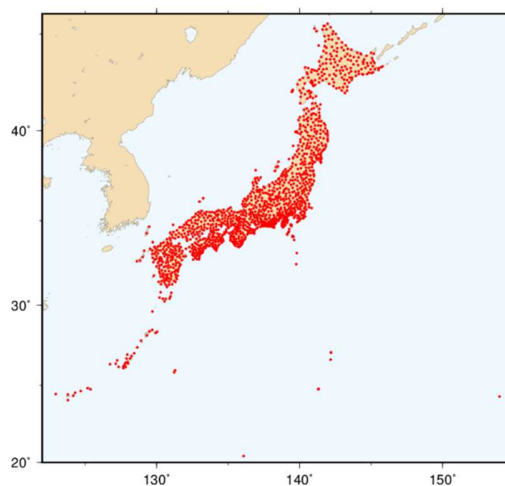


Figure 1. GEONET stations (red points)

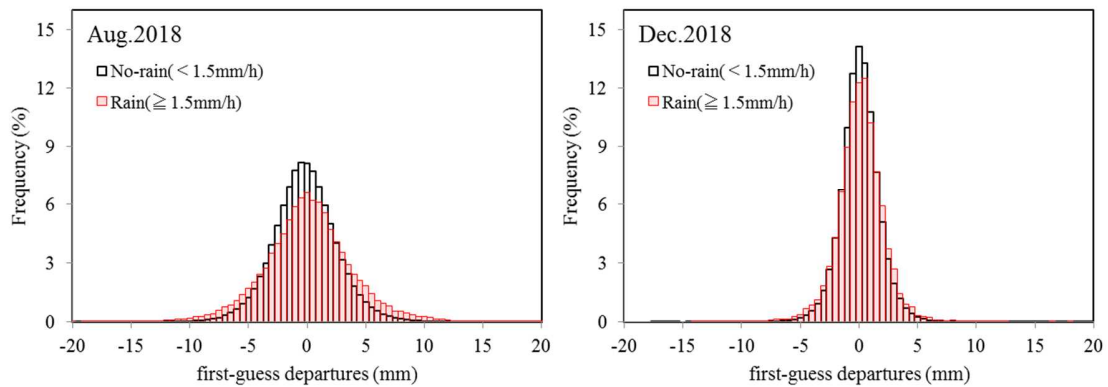


Figure 2. First-guess departures of ground-based GNSS precipitable water vapor for August (left) and December 2018 (right). Areas with  $\geq 1.5$  mm/hour of rainfall are shown in red, and those with  $< 1.5$  mm/hour are shown in white.

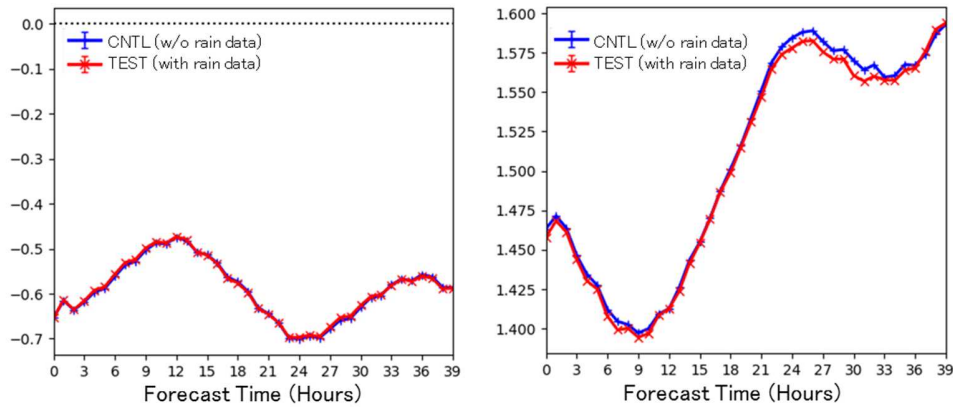


Figure 3. Mean errors (ME; left) and root mean square errors (RMSE; right) of surface specific humidity (unit: kg/kg) forecasts against observations in Japan as a function of forecast range (unit: hours) during the period from 18 June to 23 July 2018 for forecast experiments (blue lines: CNTL without rain data; red lines: TEST with rain data)

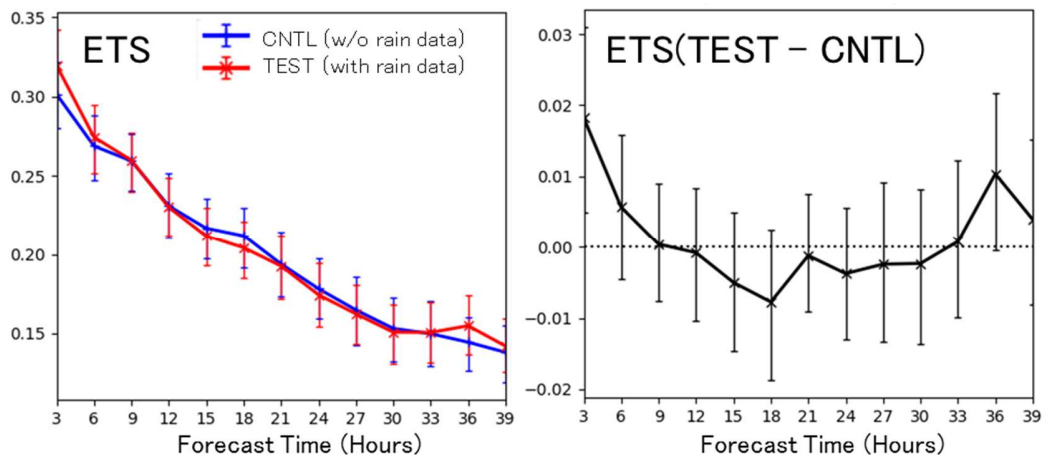


Figure 4. Equitable threat scores (ETS; left) for three-hour cumulative precipitation forecasts against Radar/Raingauge-Analyzed Precipitation during the period from 18 June 2018 to 23 July 2018 for forecast experiments (blue lines: CNTL without rain data; red lines: TEST with rain data). The figure on the right shows TEST - CNTL. Error bars represent 95% confidence intervals.

# Applying a nonlinear transformation to the analysis of surface visibility and cloud ceiling height

Runhua Yang<sup>1,2</sup>, R. James Purser<sup>1,2</sup>, Jacob R. Carley<sup>2</sup>, Manuel Pondevca<sup>1,2</sup>, Yanqiu Zhu<sup>1,2</sup>, Steven Levine<sup>2,3</sup>, Wan-Shu Wu<sup>2</sup>  
<sup>1</sup> I.M. Systems Group, Inc., <sup>2</sup> NOAA NWS/National Centers for Environmental Prediction, US  
<sup>3</sup> Systems Research Group, Colorado Springs, CO  
Email: [Runhua.Yang@noaa.gov](mailto:Runhua.Yang@noaa.gov)

## Real-Time and Unrestricted Mesoscale Analysis Systems

The Real Time Mesoscale Analysis (RTMA) and the UnRestricted Mesoscale Analysis (URMA) are 2D variational analysis systems that first went into operations at NOAA in 2006 and 2013, respectively. The systems provide gridded analyses of surface pressure, temperature and moisture at 2 meters above ground level, wind speed/direction and wind gust at 10 meters, significant wave height, ceiling height and visibility, and cloud cover for the contiguous United States (CONUS), Alaska, Hawaii, Puerto Rico, and Guam (Pondevca et al. 2011). In December of 2017, the rapid-update RTMA (RTMA-RU) system was added to the RTMA operational suite, refining the hourly-updated analysis to 15-minute-updated analysis for CONUS.

The three components of RTMA are a downscaling and first guess process leveraging short-term forecasts from the best-available convection-allowing model output (e.g., the High Resolution Rapid Refresh); an analysis process using the NOAA Grid-point Statistical Interpolation (GSI) system; and a post processing step to convert the guess and analysis into GRIB2 format, as well as estimate the analysis error using a Lanczos-based method (Pondevca et al. 2011). The system assimilates observations from a variety of platforms including surface observing systems, mesonets, buoys, geostationary satellite cloud products, scatterometer winds, and altimeter-derived significant wave heights. This paper focuses on efforts toward improving the ceiling and visibility analysis through a nonlinear transformation of the variables.

## Objective

The objective is to improve ceiling and visibility analysis by employing a nonlinear transformation technique into RTMA. Analyzing ceiling and visibility is very challenging, mainly because the fields are highly discontinuous in space and time. While poor visibility and low cloud ceiling are typically rare events, they are critically important to general aviation, commercial transportation, and helicopter emergency rescue services.

There are two advantages from this new algorithm: 1) the transformed variables better adhere to a Gaussian distribution, therefore leading to a better analysis; 2) the errors associated with the linear approximation are eliminated. In the previous algorithm, a linear approximation was required to combine the penalties calculated in logarithmic space with those calculated in the state space. The new algorithm eliminates this step because all computations in the analysis process are computed with the transformed ceiling and visibility (Yang et al. 2018).

## Nonlinear Transformation and parameter estimation

The general nonlinear transformation formula (Purser, personal communication) takes the following form:

$$G(p;x) = [x^p - 1]/p$$

Here,  $x$  is the variable to be transformed and  $p$  is a real constant. The transformation converts  $x$ , which is not a Gaussian variable, into the space of  $G(p; \cdot)$ . The transformed variable possesses a Gaussian distribution. Figure 1 shows the function family with several  $p$  values: when  $p \rightarrow 0$ ,  $G(p; x)$  is the natural logarithm function, whereas when  $p=1$ , it is a linear function.

The procedure to determine  $p$  was done empirically in the following way: given a value,  $p$  confined to a range [0-1], we apply  $G(p; x)$  to both observations and the first guess, and compute the innovation. The median of the innovations is then used to divide the data into two groups, one with values less than the median (denoted as R1), the other with values equal to or larger than the median (denoted as R2). A histogram is computed for each

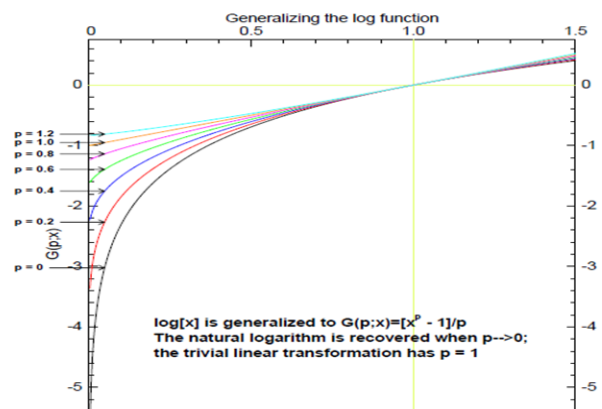


Figure 1 General nonlinear transformation function

group. The same computation is then repeated using the data set generated by  $G(p; x)$  with a different  $p$  value. Here we defined the so-called optimal  $p$  when the following criterion was satisfied: if the histogram shapes of R1 and R2 change significantly with different  $p$  values, an optimal  $p$  exists between these two adjacent values. In practice, the resulting histogram of R1 is the one closest to Gaussian distribution among all other histograms (e.g., Fig. 4 of Yang et al. 2018). In this application,  $p = 0.2$  for visibility and  $p = 0.1$  for cloud ceiling.

We analyzed data sets of the innovations from multiple RTMA analyses to obtain a range of approximate error statistics. Single observation tests were also used to check and adjust these statistics. A real-time test run spanning several months was also leveraged to adjust the statistics based on the overall analysis fits to the observations.

### Assessment and Examination of Results

The experiment run started March 2018 and continued for several months. The corresponding control run for the comparison was performed with the previous ceiling and visibility analysis algorithm used in the operations. The metrics for assessment focused on comparisons between the control and the experiment throughout examination of the overall analysis fits to observations, visual inspection of the 2D-fields, and multi-level contingency tables based on flight category definitions. A preliminary assessment shows the experimental runs produce a consistent reduction in RMSE but yield a slightly larger bias for visibility. The comparisons of 2D fields revealed that the experimental run represents the fine-scale structures of the ceiling and visibility field, particularly in areas with significant weather systems. The details are described in Carley et al. (2018). Table 1 lists the Hit Rate and False Alarm Rate computed from the observed and analyzed visibility, generated by the control and the experiment with RTMA-RU, over the CONUS for the period of 03/31 – 04/03, 2018. The Hit Rate indicates a system’s ability to detect an event of interest, while False Alarm Rate describes the fraction of events that were forecast but did not occur. The table clearly demonstrates that the experiment improves the Hit Rate and reduces the False Alarm Rate in all four flight categories for visibility. Similar improvements are found for ceiling (not shown).

**Table 1. Hit Rate and False Alarm Rate (x 100) computed from observed and analyzed visibility generated by the control and the experiment. False Alarm rate is annotated in brackets.**

	LIFR Low Instrument Flight Rules Visibility < 1 mi.	IFR Instrument Flight Rules 1 mi <= Visibility < 3	MVFR Marginal Visual Flight Rules 3 mi <= Visibility <= 5	VFR Marginal Visual Flight Rules Visibility > 5
Control	48.84 [1.34]	50.28 [1.77]	49.96 [2.32]	98.39 [10.63]
Experiment	71.99 [0.48]	70.04 [1.44]	62.10 [2.00]	98.61 [5.55]

### References

Carley, J., R. Yang, De Pondecia, M.S., R. James Purser: 2018: Assessment and Subsequent Revisions of RTMA-RU C&V Products. *AWRP Ceiling and Visibility Project Report to FAA*. 34 pp.

Pondecia, M.S., G.S. Manikin, G. DiMego, S.G. Benjamin, D.F. Parrish, R.J. Purser, W. Wu, J.D. Horel, D.T. Myrick, Y. Lin, R.M. Aune, D. Keyser, B. Colman, G. Mann, and J. Vavra, 2011: The Real-Time Mesoscale Analysis at NOAA’s National Centers for Environmental Prediction: Current Status and Development. *Wea. Forecasting*, **26**,593–612.

Yang, R., R. J. Purser, J. R. Carley, M. Pondecia, Y. Zhu, and W.Wu, 2018: Applying a general nonlinear transformation to the analysis of surface visibility and cloud ceiling height. *25th Conference on Numerical Weather Prediction*. Denver, CO, Amer. Meteor. Soc. 51.

### Acknowledgements

*Disclaimer: This research is in response to requirements and funding by the Federal Aviation Administration (FAA). The views expressed are those of the authors and do not necessarily represent the official policy or position of the FAA.*

Thanks to Michael Lueken at EMC for his continuous assistance in integrating the algorithm into GSI system. Thanks to Jenny Colavito at the FAA for her insightful comments and editing.

# Assimilation of S-NPP VIIRS Land Surface Temperature into NCEP RTMA AK Domain

Xiaoyan Zhang<sup>1,2</sup>, Jacob R. Carley<sup>1</sup>, John Derber<sup>3</sup>, Andrew Collard<sup>1,2</sup>, and Manuel Poncena<sup>1,2</sup>

1. NCEP/EMC College Park, MD, U.S.

2. IMSG, College Park, MD, U.S.

3. NCEP/EMC Retired

Email: [xiaoyan.zhang@noaa.gov](mailto:xiaoyan.zhang@noaa.gov)

## Objective and background

Over the CONUS, the 2DVar Real-Time Mesoscale Analysis (RTMA) and Unrestricted Mesoscale Analysis (URMA) system have access to a fairly dense network of conventional surface observations, especially in non-mountainous regions. However, outside of the CONUS domain, especially over Alaska (AK), the coverage of in-situ observations is relatively sparse. This complicates the creation of a high quality analysis. The assimilation of satellite observations is therefore an area that can be explored to improve the RTMA/URMA surface temperature analyses in regions of limited in-situ observations. This project is focused on the AK RTMA/URMA domain and explores the assimilation of Visible Infrared Imaging Radiometer Suite (VIIRS) satellite retrieved Land Surface Temperatures (LST) to improve the AK RTMA/URMA surface 2-meter temperature analysis (T2M). This 3-km resolution surface analysis is expected to contribute to improving forecasters' analysis of AK weather. Previously, Bosilovich et al. (2007) showed that LST assimilation improves estimates of 2-meter air temperature, both in the mean and variability. But their study was made with a coupled land surface model.

## Methods

Previous investigations (Bosilovich et al. 2007; Reiche et al. 2010) on the assimilation of satellite retrieved LST have been mostly carried out within a pure soil model or within a coupled land surface model. Relationships between the LSTs and surface energy cycle are derived from these models. However, the RTMA/URMA is a 2DVar system; there is no coupled land surface model, or 3-D atmospheric profiles available in the analysis algorithm. It is therefore difficult to assimilate LST directly through the surface energy cycle. An alternative approach in assimilating LSTs into the RTMA/URMA system is to convert LST to T2M (also known as pseudo T2M), which can then be assimilated in the same manner as other conventional T2M observations, such as those observed from METARs. The Monin-Obukhov similarity theory, which is based on the Dyer and Hicks (1970) formula, is adopted to convert the LST to pseudo T2M in this work. The similarity theory and conversion from LST to T2M are described below in detail.

Temperature at the 2-meter height can be obtained using the similarity theory as follows:

$$T_z = \left[ \theta_g + (\theta_s - \theta_g) \times \frac{\Psi_{T_z}}{\Psi_T} \right] \left( \frac{P_{sfc}}{1000} \right)^{\frac{R}{C_p}}$$

$\theta_s$  is potential temperature at the model lowest sigma level and  $\theta_g$  is potential temperature on the ground, which is converted from LST.  $P_{sfc}$  is surface pressure. The stability functions are given by:

$$\Psi_T = \log\left(\frac{h_s}{z_0}\right) - \Psi_h; \quad \Psi_{T_z} = \log\left(\frac{z}{z_0}\right) - \Psi_{hz}$$

where  $h_s$  is the height of at the lowest model level, and  $z=2m$  is the height at which the temperature will be computed.  $z_0$  is the roughness length prescribed in the model. The ideal gas constant ( $R$ ) is  $287.04 \text{ JK}^{-1}\text{kg}^{-1}$ , and the specific heat at constant pressure ( $C_p$ ) is  $1004.0 \text{ JK}^{-1}\text{kg}^{-1}$ .  $\Psi_h$  and  $\Psi_{hz}$  are the stability function for heat but are calculated at the lowest model level and at the 2-m height above the ground, respectively. This stability function is determined according to atmospheric stability based on the Bulk Richardson number (Lee et al. 2005).

## Preliminary Results

Two single analysis experiments were performed. The control run (CTRL) only assimilates conventional

observations, as in the operational RTMA. The experiment assimilates VIIRS LST and conventional observations (EXPLST). Both experiments use the same downscaled 13-km Rapid Refresh model 1-hour forecast as the first guess. Due to its high resolution (750m), VIIRS LST was thinned to a 20-km mesh using the existing thinning scheme in GSI. All other conventional observations are kept at their original resolution. The observation error of LST is set to 1.2 Kelvin. The VIIRS LST high quality flagged pixels are used as the quality control. A gross error/outlier check is also employed in the 2DVar algorithm.

The departures of observations (pseudo T2M) from the background (OMB) and from the analysis (OMA) are shown in Fig. 1. For the cases examined here all histograms of OMA are more Gaussian than OMB. This indicates that the analysis algorithm is functioning as expected by fitting VIIRS pseudo T2M. The T2M analysis differences between EXPLST and CTRL (Fig. 2a) show mostly negative values, indicating that assimilating LST made the T2M colder than only assimilating the conventionally available in-situ observations. Consistent with the colder T2M, the 2-m dew-point temperature is also lower (Fig. 2b). Case studies beyond those described in this report have been carried out. It is confirmed that the analysis algorithm developed for the assimilation of VIIRS LST is able to fit the observations reasonably well. The standard deviation of analysis departures are reduced as expected.

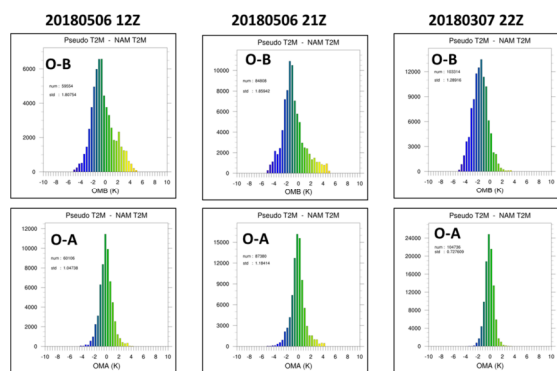


**Figure 1.** The histogram plots for departure of VIIRS LST pseudo T2M and model first-guess T2M (OMB) and analysis (OMA).

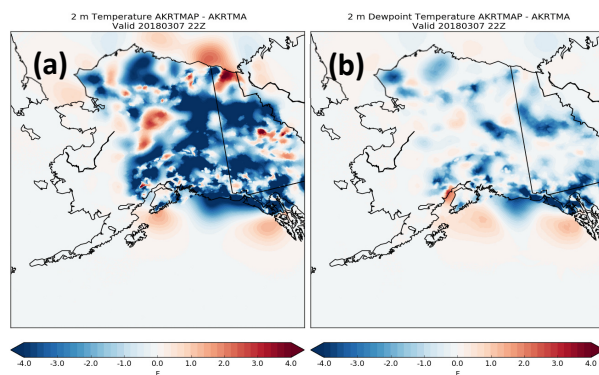


**Figure 2.** RTMA analysis difference between experiment EXPLST and CTRL for T2M (a), and 2- meter dew-point temperature (b).

## References

- Dyer, A. J., and B. B. Hicks, 1970: Flux-gradient relationships in the constant flux layer. *Quart. J. Roy. Meteor. Soc.*, **96**, 715-721.
- Bosilovich, M., J. Radakovich, A. da Silva, R. Todling, and F. Verter, 2007: Skin temperature analysis and bias correction in a coupled land-atmosphere data assimilation system. *J. Meteor. Soc. Japan*, **85A**, 205-228.
- Lee, S. J., D. F. Parrish, and W.-S. Wu, 2005: Near-surface data assimilation in the NCEP Gridpoint statistical-interpolation system: Use of land temperature data and a comprehensive forward model. NCEP office Note #446.
- Reichle, R.H., S.V. Kumar, S.P. Mahanama, R.D. Koster, and Q. Liu, 2010: Assimilation of Satellite-Derived Skin Temperature Observations into Land Surface Models. *J. Hydrometeorol.*, **11**, 1103-1122.

## Acknowledgments

Yuling Liu (NESDIS) is acknowledged for his support for processing the VIIRS LST data. to the authors are grateful to Eugene Petrescu and Emily Niebuhr in the NWS Alaska Regional office for their support for this project and their insightful comments on this study.

## Assimilation of cloudy ATMS radiances at NCEP

Yanqiu Zhu, George Gayno, R. James Purser, Xiujuan Su, Runhua Yang  
I.M. Systems Group, Inc., NOAA/NCEP/Environmental Modeling Center, College Park, Maryland  
Email: Yanqiu.Zhu@noaa.gov

In the past decade, with the advances of forecast models and the improvement of radiative transfer models, Numerical Weather Prediction centers have made steady progress towards utilizing cloudy radiances in addition to clear sky radiance observations (Geer et al. 2018). In the Gridpoint Statistical Interpolation (GSI) analysis system at the National Centers for Environmental Prediction (NCEP), the assimilation of cloudy radiances from the Advanced Microwave Sounding Unit-A (AMSU-A) microwave radiometer for ocean fields of view (FOV) became operational in the 4D hybrid Ensemble-Variational (EnVar) Global Forecast System (GFS) in 2016 (Zhu et al. 2016). Since then, an effort has been made in the expansion of the all-sky approach to use radiances from the Advanced Technology Microwave Sounder (ATMS). This work is currently being included in a real-time parallel for an upcoming operational implementation in 2019, and more detailed information can be found in Zhu et al. 2019.

ATMS has 22 channels and combines most of the channels from AMSU-A and the Microwave Humidity Sounder (MHS). With the MHS-like channels, this work also introduces water vapor channels into the all-sky approach. Normalized cloud water is used as the cloud control variable. Total cloud water is decomposed into liquid and ice cloud state variables based on a temperature-dependent empirical function. Only the radiances affected by non-precipitating clouds and clear-sky radiances are used, due to the lack of a snow and precipitation first guess from the original operational forecast model. The background error covariance is composed of the static term and another part generated from the ensemble forecasts, with 87.5% weight given to the ensemble part.

Since ATMS has varied beam widths, the ATOVS and AVHRR Pre-processing Package (AAPP, NWP SAF/EUMETSAT) with remapping and spatial averaging is applied to all 22 channels, instead of just channels 1–16 in the operational GFS system, to convert the beam widths to  $3.3^\circ$  in the all-sky approach. It has also been noticed in this study that ATMS radiances have large departures from the first guess (OmF) around coastlines and cryosphere boundaries. The capability of modeling surface properties (including land/sea fraction) based on the FOV size and shape is exercised for the all-sky ATMS radiances, and the ATMS radiances over mixed surface type locations are excluded.

With the introduction of MHS-like channels into the all-sky framework, the scattering effect increases due to the higher frequencies. In the CRTM, however, non-precipitating clouds (cloud liquid water and cloud ice) are assumed to be small particles in comparison to microwave wavelengths; thus the scattering is not considered by design when there is no information about snow, graupel and precipitation. Considering the consistency between the observations and simulated radiances from the CRTM, a new observation scattering index (SI) is constructed to exclude those radiances that are affected by strong scattering. SI is defined as the difference in cloud effects between channels 16 and 17, where the cloud effect is calculated as the difference between the observed brightness temperature and the brightness temperature without hydrometeor information being considered. Observations from channels 1–7 and 16–22 with  $|SI| > 10.0K$  are excluded in this study. In the final gross error check, bias-corrected ATMS radiances with OmF magnitude larger than 10.0K or three times the observation error, whichever is smaller, are excluded from the data assimilation system.

The ATMS radiances that pass the quality control procedures are bias corrected in the GSI's variational bias correction framework (Derber and Wu 1998; Zhu et al. 2014), but by using a selected data sample in the bias coefficient derivation to avoid the impact of large model errors. The observation error of the ATMS radiance is assigned as a function of the symmetric cloud amount (Geer and Bauer 2011) followed by the situation-dependent observation error inflation procedure (Zhu et al. 2016), where the two most important physically-

based factors are cloud placement difference and cloud liquid water difference between the first guess and observation.

Overall, the assimilation of ATMS radiances in the all-sky approach improves the consistency of microwave radiance OmFs among different sensors. An example is given in Fig. 1 with ATMS channel 16 and its closest matches: MHS channel 1 and AMSU-A channel 15. The bias correction is seen to have a big impact on the OmF patterns. After bias correction, while the OmF patterns for ATMS channel 16 and MHS channel 1 are similar in the clear-sky approach, they are significantly different in several regions from the OmF patterns of ATMS channel 16 and AMSU-A channel 15 in the all-sky approach. One such region is to the west of the South American continent. Issues are identified in the clear-sky approach of operational MHS and ATMS radiance assimilation, with the possible leaking of radiances affected by clouds into the GSI or an incomplete removal of cloud effects. As a small improvement in the fits to rawinsonde specific humidity data is observed to persist in the 48h forecast, the assimilation of all-sky ATMS radiances is found to have an overall neutral impact on the model forecast skill, with a small improvement in the Southern Hemisphere mainly at day 3. The all-sky ATMS radiance assimilation will become operational in the upcoming GFS implementation in 2019.

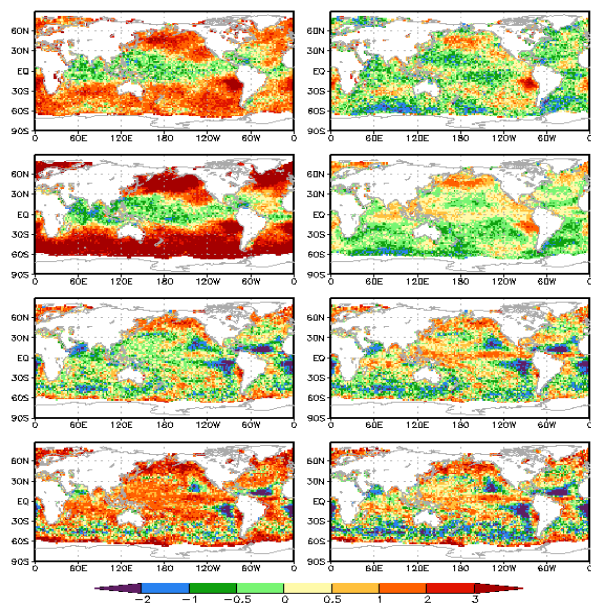


Figure 1 One-month averaged OmF over water of June 2015: before (left column) and after (right column) bias correction for MHS channel 1 (row 1) and ATMS channel 16 (row 2) in the clear-sky approach, and ATMS channel 16 (row 3) and AMSU-A channel 15 (row 4) in the all-sky approach. The unit is K.

Although initial efforts made to account for the non-Gaussian distribution of innovations using an adaptation of variational quality control based on a super-logistic distribution (Purser 2018) have not so far been successful, future work will continue on this topic. Since the all-sky AMSU-A and ATMS radiance assimilation are currently implemented only over ocean FOVs, a research study on the all-sky radiance assimilation over land is also underway. As the forecast models are transitioning to the Finite-Volume Cubed-Sphere Dynamical Core (FV3) model with more advanced physics at NCEP, the choice of cloud control variables will be examined. Meanwhile, the tests on the inclusion of subgrid-scale clouds and precipitation in the all-sky radiance assimilation are ongoing.

## References

- Derber, J. C. and W.-S. Wu, 1998: The use of TOVS cloud-cleared radiances in the NCEP SSI analysis system. *Mon. Wea. Rev.*, 126, 2287-2299.
- Geer, A. J., K. Lonitz, P. Weston, M. Kazumori, K. Okamoto, Y. Zhu, E.H. Liu, A. Collard, W. Bell, S. Migliorini, P. Chambon, N. Fourrie, M-J Kim, C. Kopken-Watts, C. Schraff, 2018: All-sky satellite data assimilation at operational weather forecasting centres. *Q. J. R. Meteorol. Soc.*, 144,1191-1217.
- Geer, A.J. and P. Bauer, 2011: Observation errors in all-sky data assimilation. *Q. J. R. Meteorol. Soc.*, 137, 2024-2037.
- Purser, R.J, 2018: Convenient parameterization of super-logistic probability models of effective observation error. NOAA/NCEP Office Note 495. <https://doi.org/10.25923/kvmz-vf34>, 8pp.
- Zhu, Y., J. Derber, A. Collard, D. Dee, R. Treadon, G. Gayno, J. A. Jung, 2014: Enhanced radiance bias correction in the National Centers for Environmental Prediction's Gridpoint Statistical Interpolation Data Assimilation System. *Q. J. R. Meteorol. Soc.*, 140, 1479-1492.
- Zhu, Y., E. Liu, R. Mahajan, C. Thomas, D. Groff, P. van Delst, A. Collard, D. Kleist, R. Treadon, J. Derber, 2016: All-sky microwave radiance assimilation in NCEP's GSI analysis system. *Mon. Wea. Rev.*, 144, 4709-4735.
- Zhu, Y., G. Gayno, J. R. Purser, X. Su, R. Yang, 2019: Expansion of the all-sky radiance assimilation to ATMS at NCEP. *Mon. Wea. Rev.*, <https://doi.org/10.1175/MWR-D-18-0228.1>